Translithospheric Mantle Diapirism: Geological Evidence and Numerical Modelling of the Kondyor Zoned Ultramafic Complex (Russian Far-East)

J.-P. BURG[1]*, J.-L. BODINIER[2], T. GERYA[1], R.-M. BEDINI[2], F. BOUDIER[2], J.-M. DAUTRIA[2], V. PRIKHODKO[3], A. EFIMOV[4], E. PUPIER[2] AND J.-L. BALANEC[2]

[1]EARTH SCIENCES DEPARTMENT, ETH ZENTRUM AND UNIV. ZÜRICH, SONNEGGSTRASSE 5, ZÜRICH, 8092, SWITZERLAND

[2]GÉOSCIENCES MONTPELLIER, UNIVERSITÉ DE MONTPELLIER 2 & CNRS, CC 60, PLACE EUGÈNE BATAILLON, 34095 MONTPELLIER CEDEX 05, FRANCE

[3]INSTITUTE OF TECTONICS AND GEOPHYSICS, RUSSIAN ACADEMY OF SCIENCES, 680063 KHABAROVSK, RUSSIA

[4]INSTITUTE OF GEOLOGY AND GEOCHEMISTRY, RUSSIAN ACADEMY OF SCIENCES, 620151 EKATERINBURG, RUSSIA

We report new structural, microstructural, petrological, and major- and trace-element data on ultramafic rocks from the Kondyor zoned ultramafic complex in Far-East Russia. The ultramafic rocks are subdivided into three subconcentric lithologies, from core to rim: (1) a metasomatic domain where generally phlogopite-rich dykes pervasively intrude dunite; (2) a main dunite core; (3) a pyroxenite rim. The ultramafic rocks have nearly vertical contacts with the surrounding Archaean basement (gneisses, quartzites and marbles) and hornfelsed Riphean sediments. The hornfelsed sediments show a relatively steep (>60°), outward dipping layering, which rapidly flattens to horizontal away from the inner contact. Although the Riphean sediments define a dome-like structure, the inward, shallow dipping foliation of the dunites indicates a synformal structure. Detailed petro-structural investigations indicate that the Kondyor dunites were deformed by solid-state flow under asthenospheric mantle conditions. The outward textural change from coarse- to fine-grained equigranular dunite and the outward-increasing abundance of subgrains and recrystallized olivine grains suggest dynamic recrystallization while fluid circulation was channelized within the core metasomatic zone, with a decreasing melt fraction from core to rim, and also suggest that solid-state deformation induced grain-size reduction towards the cooling border of the Kondyor massif. Based on their geochemistry, the dunites are interpreted as mantle rocks strongly affected by reaction with melts similar to the Jurassic–Cretaceous Aldan Shield lamproites. Rim pyroxenites were formed by a melt-consuming peritectic reaction, implying the existence of at least a small, conductive thermal gradient around the dunite body while the latter was still at near-solidus temperature conditions. This suggests that the zoned structure of Kondyor was initiated at mantle depths, most probably within the subcontinental lithosphere. Upon cooling, the lamproitic melts were progressively focused in the central part of the massif and drained into vein conduits where they reacted with the wall-rock dunite. Two-dimensional numerical modelling based on finite-differences with a marker-in-cell technique incorporates temperature-dependent rheologies for both molten and non-molten host rocks. The modelling consolidates the structural, petrological and geochemical interpretations, which show that the dunites represent the synformal, flat-lying apex of an asthenospheric

*Corresponding author. Telephone: +41 44 632 6027. Fax: +41 44 632 1030. E-mail: jean-pierre.burg@erdw.ethz.ch

mantle diapir, triggered by fluid pressure channelized in the core, which nearly reached the Earth's surface. We conclude that translitho-spheric mantle diapirism is an important mode of mass transfer in the Earth.

INTRODUCTION

Zoned ultramafic complexes (ZUCs) consist of relatively small bodies that expose a dunite core surrounded by successive shells of wehrlite–pyroxenite, hornblendite and, in some cases, felsic rocks (e.g. Wyllie, 1967; Kelemen & Ghiorso, 1986). ZUCs are found in both subduction-related (Alaskan-type complexes) and intracontinental rift (alkaline–ultramafic complexes) settings, and are commonly interpreted as ultramafic igneous intrusions emplaced at crustal level (e.g. Irvine, 1967; Veksler *et al.*, 1998; Batanova *et al.*, 2005). Subduction-related ZUCs form linear belts and are surrounded by large gabbroic bodies (e.g. Taylor, 1967; Efimov *et al.*, 1993; Jagoutz *et al.*, 2006). Intraplate ZUCs are associated with alkaline and locally subalkaline magmatic rocks (e.g. Butakova, 1974) but are generally not related to large gabbro intrusions. ZUCs have been ascribed to five pro-cesses: (1) multiple intrusions with new, successive magma batches intruded into earlier intrusions (e.g. Ruckmick & Noble, 1959; Taylor, 1967); (2) antiformal folding of strati-form cumulates (e.g. Irvine, 1967, 1974); (3) flow differentia-tion, with early crystals entrained into the center of a moving magma body (e.g. Bhattacharji & Smith, 1964; Findlay, 1969; James, 1971); (4) stepwise reaction between pre-existing ultramafic wall-rocks and later magmas (e.g. Kelemen & Ghiorso, 1986); (5) melt channels reaching into the mantle (e.g. Murray, 1972; Burg *et al.*, 1998; Jagoutz *et al.*, 2006).

This study is focused on the zoned ultramafic complex of Kondyor, in Far-East Russia (Fig. 1), which Russian Earth scientists have studied in great detail because it contains exceptional platinoid ore deposits (e.g. Nekrasov *et al.*, 1991; Cabri & Laflamme, 1997; Malitch, 1999; Shcheka *et al.*, 2004). Like many other intra-plate ZUCs, Kondyor exhibits several features that are difficult to explain in terms of an igneous origin. First, the concentric arrange-ment of dunite core–pyroxenite rim and the outward decrease of Mg-number $[=100 \times Mg/(Mg + Fe)]$ in the dunites imply that, against general logic, magma crystalli-zation proceeded from the centre outward. Second, a cumulate origin for the dunites with high Mg-number (mostly >89) requires unrealistically large volumes of residual melt whereas only minor igneous intrusions are found in the body. Finally, there is a mechanical problem

in explaining how high-density rocks can rise from mantle depths and be emplaced in the upper crust.

New field, structural, petrographic and geochemical evi-dence supports the conclusion that the zoned ultramafic complex of Kondyor represents a solid intrusion of mantle rocks at the apex of a mantle 'diapir'. To resolve the mechanical problem of how high-density rocks can rise into low-density, upper crustal sequences, we employed a two-dimensional (2D) numerical modelling approach to constrain the thermo-mechanical processes involved in the emplacement of peridotite intrusions such as Kondyor. Our results support the interpretation of the Kondyor ZUC as a translithospheric intrusion. The modelling fur-ther shows that translithospheric diapirism does not need regional tectonics to take place, but instead a rheological perturbation that acts as a magma channel. We conclude that the process should be common and may explain some of the crater-like features on the ancient Earth and on other terrestrial planets.

GEOLOGICAL SETTING OF THE KONDYOR ULTRAMAFIC BODY

Several alkaline–ultramafic zoned complexes have intruded the Precambrian rocks of the Aldan Shield (southeastern Siberia) during Mesozoic rifting (e.g. Butakova, 1974; Elianov & Andreev, 1991; Malitch, 1999). One of them, the Kondyor ZUC, occurs in the eastern part of the shield as a circular, crater-like structure centred at 57°37'10ʺN, 134°39'12ʺE, which is isolated amid flat-lying, very low metamorphic grade clastic sediments of Riphean and Late Proterozoic age that form the uncon-formable cover of the crystalline basement (Khain, 1985; Elianov & Andreev, 1991). The Late Jurassic–Early Cretaceous age of the Kondyor ZUC has been inferred from phlogopite K–Ar dating of dunites (149–137 Ma) and pyroxenites (124–113 Ma), and whole-rock, feldspar, mica and amphibole K–Ar ages of alkaline gabbros (120–83 Ma) and nepheline-syenite pegmatites (130–110 Ma; references have been given by Orlova, 1992; Kononova *et al.*, 1995). These ages were substantiated by Pushkarev *et al.* (2002), who obtained K–Ar ages of 132 ± 8 and 115 ± 6 Ma for an ultramafic rock and a gabbro, respectively, and a Rb–Sr age of 123 ± 2 Ma for a pyroxenite. The ages reported for Kondyor are consistent with K–Ar and Rb–Sr ages obtained on the related Inagli ZUC, further to the west (Mues-Schumacher *et al.*, 1996). However, osmium isotope data give a mantle model age of 330 ± 30 Ma for Kondyor (Malitch & Thalhammer, 2002).

The Kondyor ZUC is composed of a chromite-bearing dunite core, *c.* 5·5 km in diameter, surrounded by an irregu-lar, 100–750 m wide, composite aureole of wehrlites and oli-vine-bearing clinopyroxenites in its inner part and of
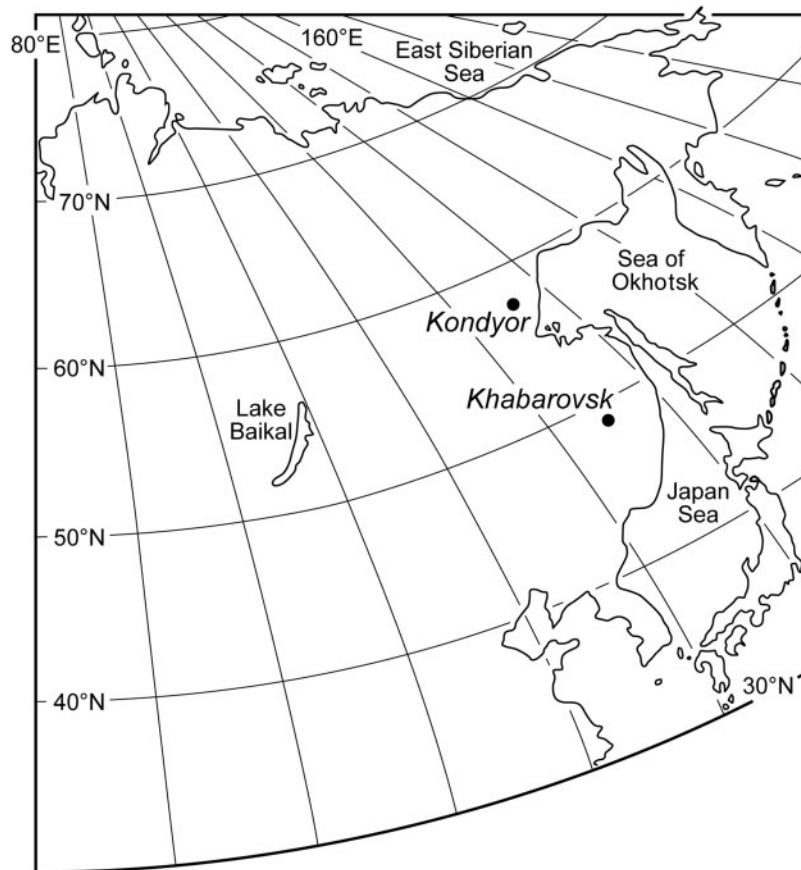
Fig. 1. Location of the Kondyor Massif in Far-East Eurasia.

magnetite–amphibole (± plagioclase) clinopyroxenites in the outer rim (Fig. 2). The dunites are cut by a variety of igneous rocks ranging from an early network of metasomatic veins (glimmerites and phlogopite–richterite–apatite–carbonate and Fe–Ti-oxide clinopyroxenites) to later dikes of magnetite-rich clinopyroxenite ('koswite'), amphibole-gabbros and syenites. Multiple, crescent-shaped and locally strongly deformed intrusions of sub-alkaline gabbro are occasionally intercalated between the ultramafic body and the metamorphic country rocks. Intrusions of diorite and monzodiorite occur around the massif and extend out as large apophyses into the Riphean country rocks (Fig. 2).

Fault-bounded panels of gneiss, amphibolite, schist, quartzite and marble represent the dislocated Aldan Shield basement in an up to 500 m wide outer ring that separates the circular, concentrically zoned ultramafic massif from the surrounding sedimentary cover (Fig. 2). Contact metamorphism is recognized in a 500–3000 m wide aureole of hornfelsed Riphean sediments (Orlova, 1992) ranging from partial melting (Fig. 3e) at the contact with pyroxenites and gabbros

through garnet–corundum–sillimanite gneisses and skarns to very low-grade metasediments. The crater-like morphology of Kondyor results from the erosion-resistant hornfels rocks forming an annular ridge around the more deeply eroded ultramafic core (Kharkevich & Krot, 1985). Hornfels xenoliths also occur in the centre of the ultramafic body. Erosion of the upper part of the ZUC has produced platinoid element-rich placer sediments, which accumulated *in situ* within the 'crater'.

Gravimetric and magnetic data emphasize the asymmetric distribution of lithologies, with strong anomalies over the magnetite-rich metasomatic domain in the WSW sector of the dunite core. Modelling of the gravimetric data suggests that the ultramafic rocks extend as a cylindrical, sub-vertical body down to a depth of at least 10 km (Efimov & Tavrin, 1978).

Lithologies

Field, structural, mineralogical and geochemical studies were focused on the ultramafic rocks and related igneous intrusions. The ultramafic rocks are subdivided into three

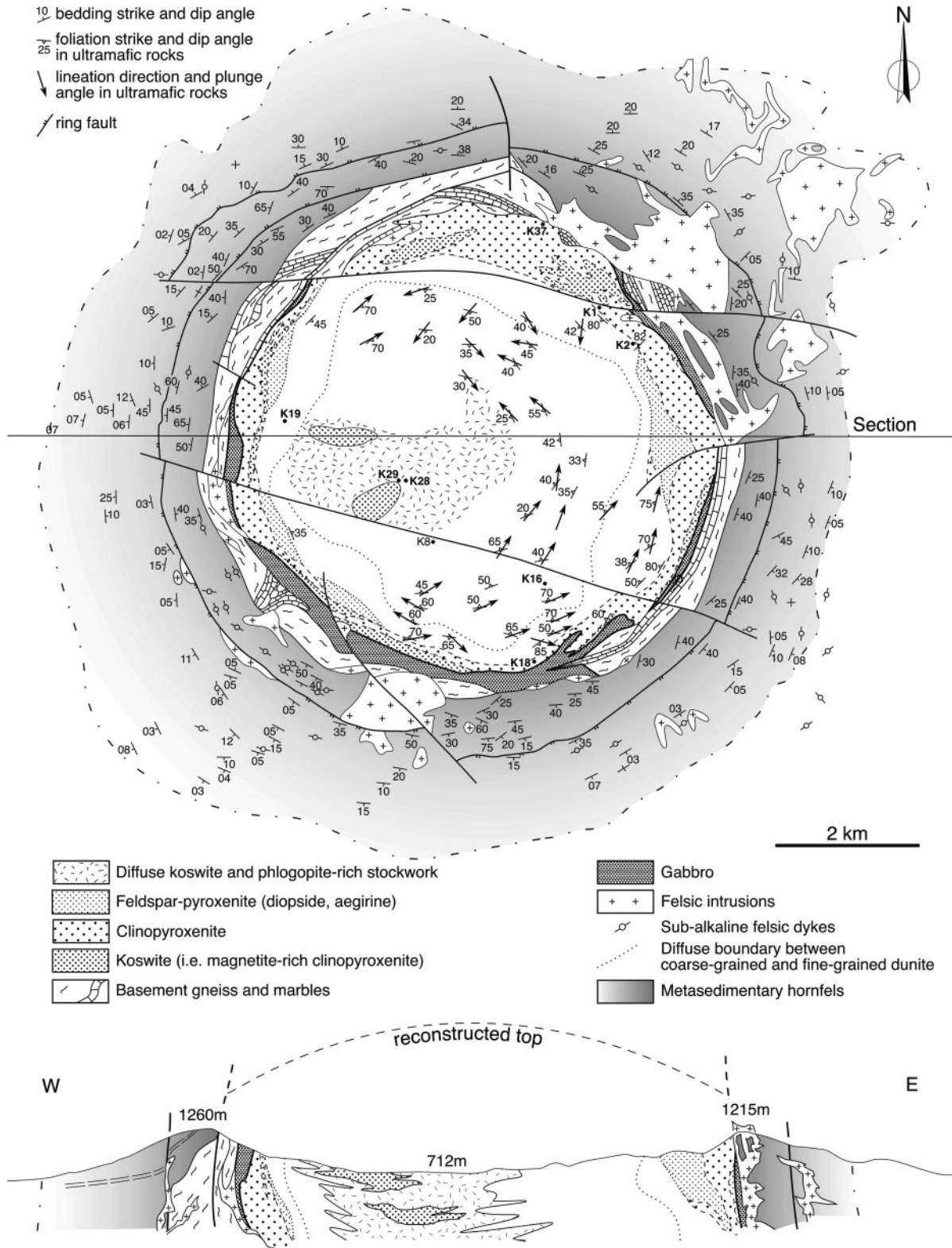**Fig. 2.** Geological map and cross-section (vertical scale = horizontal scale) of the Kondyor body, synthesized after Orlova (1992), Zemlyanukhin & Prikhodko (1997) and the authors' own data. The center of the crater-like structure is near 57°35′15″N, 134°39′20″E. Only samples referred to in the text (with prefix K) are marked, for sake of legibility. The locations of other samples listed in Tables 1–3 are given in the Appendix.
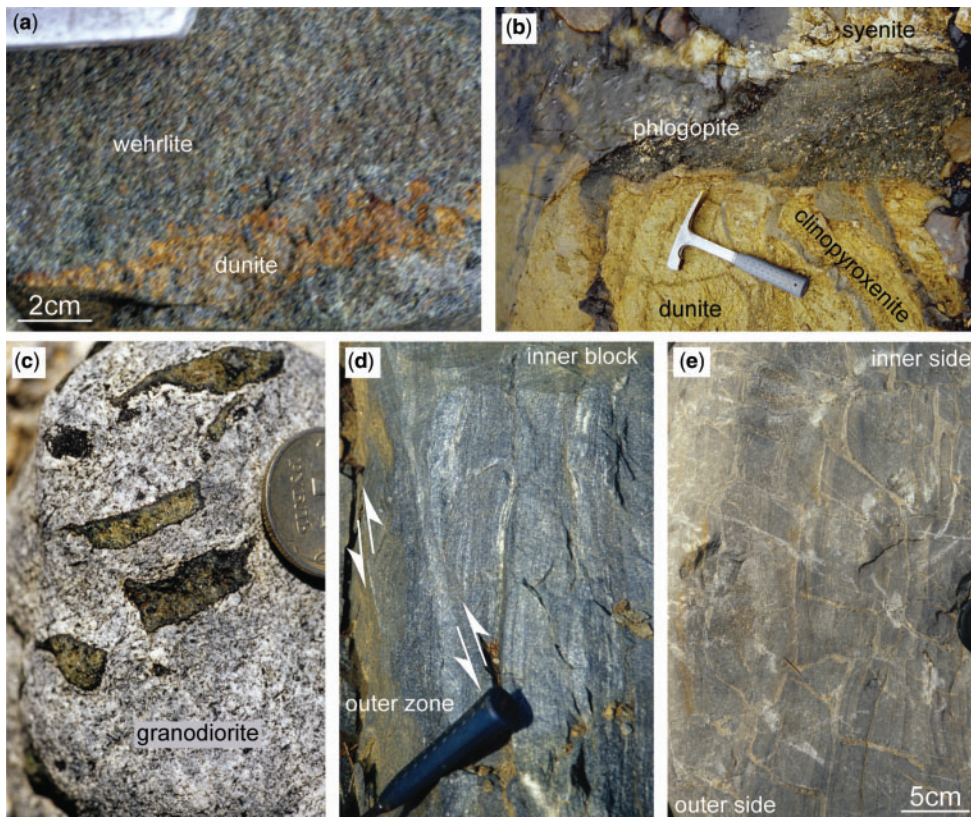
Fig. 3. Field relationships between lithologies. (a) Dunite flame in rim wehrlite (top left = top of hammer for scale) at 57°36′25″N, 134°40′46″E; (b) clinopyroxenite dyke cut by a phlogopite-rich and a syenite dyke at 57°35′34″N, 134°38′44″E; (c) spinel-bearing forsterite–phlogopite xenoliths in a peripheral subalkaline granodiorite (boulder); (d) ductile shear bands seen parallel to the down-dip lineation indicating right-side up (white arrows show relative movement) with respect to the left-side country rocks at 57°37′09″N, 134°39′53″E; (e) hornfelsed Riphean sediments with (subvertical) layer-parallel and across-bedding leucosomes indicating partial melting at 57°34′29″N, 134°42′04″E.

units: (1) the main dunite core; (2) the pyroxenite rim; (3) a metasomatic domain.

Dunite core

The dunite texture varies from coarse-grained (2–3 cm), sometimes tabular, in the core to fine-grained against the rim contact. The dunites with coarse-grained, tabular textures are comparable with the 'coarse-granular' cratonic mantle xenoliths from kimberlites whereas the texture of the fine-grained dunite is typical of 'mantle tectonites' (Boullier & Nicolas, 1973). Away from the pyroxenite rim and the metasomatic domain, with the exception of a few chromite schlieren and segregations, the main dunite has a homogeneous modal and mineral composition (Tables 1 and 2). In addition to olivine (89·5–91% Fo; Table 2), the dunites contain subordinate chromite (44–54% Cr_2O_3; Table 2), either as inclusions in olivine or as interstitial, euhedral crystals. Large, poikiloblastic crystals of chromite are rare. Some dunites contain minute amounts of

phlogopite coating the surfaces of chromite grains and interstitial, high-Mg-number, Cr-diopside [Mg-number = $Mg/(Mg + Fe^{2+})$ cationic ratio ~0·95; Table 1].

Rim pyroxenites

The transition from dunite to pyroxenite is gradual over several centimetres to a few tens of metres and shows textural evidence for replacement of the dunite by pyroxenite. Approaching the rim pyroxenites, the dunites are first enriched in Cr-diopside veinlets and seams (clinopyroxene-bearing dunites) and then grade into (1) wehrlites containing 'residual' flames of chromite-bearing dunite (Fig. 3a); (2) wehrlites and olivine-clinopyroxenites where deformed olivine occurs as inclusions in poikiloblastic, chromium-rich diopside (Fig. 4; sample K2, Fig. 2; Tables 1 and 2); (3) clinopyroxenites composed of Cr-free diopside and spinel showing zoning from residual chromite cores to (Ti-)magnetite and/or ilmenite rims (sample K1, Fig. 2; Tables 1 and 2); (4) Fe-rich clinopyroxenites composed of

Table 1: Rock classification and mineralogy

Structural domains and rock types	Mineralogy	Samples
Main dunite core		
Dunites	**olivine**, Cr-spinel, ± clinopyroxene (diopside)	8192, 8198, 8201, 8226, 8304, 8305, 8308, 8319, 8323, 8388, 8398, 8403, 8408, 8409, K8, K12, K16, K19, K23
Wehrlite, clinopyroxenite rim and related gabbros or syenites		
Wehrlites	**olivine**, **clinopyroxene** (diopside), zoned oxides (Cr-spinel to Ti-magnetite, from core to rim), ± phlogopite	K2, K3, K4
Clinopyroxenites	**clinopyroxene** (diopside to augite), Ti-magnetite, phlogopite, ± olivine, ± amphibole	8276, 8302, 8439, 8443, K1, K18, K35, K37
Gabbros	**clinopyroxene** (augite), **plagioclase**, Ti-magnetite, ± amphibole, ± biotite	8235, 8266, 8385
Nepheline syenite	**K-feldspar**, plagioclase (albite), clinopyroxene (aegirine), nepheline	K21
Metasomatic domain		
Dunite	**olivine**, Cr-spinel	K27
Phlogopite dunites	**olivine**, zoned oxides (Cr-spinel to Ti-magnetite, from core to rim), phlogopite, ± clinopyroxene (diopside), ± richterite, ± rutile (traces)	120d, 121d, 141, 141d, 142a, 142b, 143 (samples from drill cores), K28, K29
Composite, glimmerite and phlogopite–richterite clinopyroxenites (veins)	**clinopyroxene** (endiopside and aegirine augite, diopside associated with calcite), **phlogopite**, **richterite**, apatite, calcite, zoned oxides (magnetite to Ti-magnetite, from core to rim), ilmenite (exsolutions in oxides), Cr-spinel, titanite, perovskite, rutile	120p, 121p (samples from drill cores), K6
Phlogopite, apatite and Ti- magnetite clinopyroxenites (intrusive bodies)	**clinopyroxene** (augite), **apatite**, **phlogopite**, **Ti-magnetite**, ± amphibole (kaersutite)	8253, 8258, 8375, K26
Late dykes		
Koswites	**clinopyroxene** (augite), **(Ti-)magnetite**, **apatite**, amphibole (kaersutite)	K7, K9
Amphibole gabbros	**amphibole**, **clinopyroxene**, **plagioclase**, ± magnetite	8486, 8491
Nepheline syenite	**plagioclase** (albite), clinopyroxene (aegirine), nepheline	8216

Predominant minerals are shown in bold.

augitic pyroxene and Ti-magnetite (sample K37, Fig. 2; Table 2). This variation is coupled with a textural change from fine-grained textures reminiscent of mantle tectonites (cpx-bearing dunites and wehrlites with olivine flames) to coarse-grained cumulate textures (clinopyroxenites), through poikiloblastic, replacive textures (wehrlites). It is also accompanied by a gradual decrease of the Fo content of olivine and of the Mg-number of clinopyroxene (Table 2). Fo in olivine decreases from 89·5–91% in dunites to 86–87% in the K2 wehrlite and 65–70% in interstitial olivine of the Fe-rich K18 clinopyroxenite. The Mg-number of cpx decreases from ∼0·95 in dunites to ∼0·92 in wehrlites and ∼0·85 in Fe-rich clinopyroxenes

(Table 1). All rim pyroxenites contain small amounts of interstitial phlogopite and the Fe-rich pyroxenites may also contain pargasitic amphibole.

Gradual transitions are observed between the cumulate clinopyroxenites and the peripheral intrusions of alkaline gabbros, via magnetite clinopyroxenites containing feldspar (microcline) veins and sparse andradite.

Metasomatic domain

The metasomatic domain is an area of about 5 km^2 in the WSW part of the Kondyor massif (Fig. 2), where the dunite is cut by a very dense network of veins of glimmerite and

Table 2: Representative compositions of minerals from Kondyor ultramafic rocks

	Olivine						
	Main dunite core		Wehrlite/clinopyroxenite rim		Metasomatic domain (phlogopite dunites)		
Sample:	K8	K12	K2	K1	drill cores		
n:	11	5	20	2	2	2	2
wt %							
SiO$_2$	40·75	40·11	40·01	37·34	40·82	40·54	39·45
FeO	8·58	9·80	12·56	27·62	8·93	9·83	15·62
MnO	0·19	0·21	0·25	0·41	0·19	0·22	0·20
MgO	49·43	48·83	46·38	34·27	49·68	48·81	44·25
NiO	0·19	0·10	0·12	0·07	0·19	0·16	0·07
CaO	0·27	0·23	0·12	0·03	0·14	0·19	0·12
Sum	99·41	99·29	99·45	99·74	99·95	99·76	99·70
Fo (%)	90·95	89·68	86·58	68·54	90·66	89·63	83·29

	Amphibole				
	Metasomatic domain				
	(glimmerite veins)		(clinopyroxenite veins)		
Sample:	drill cores				
n:	8	5	2	8	2
wt %					
SiO$_2$	56·52	55·28	55·02	55·99	53·52
TiO$_2$	0·49	0·86	0·39	0·73	0·72
Al$_2$O$_3$	0·59	1·30	1·50	0·68	2·52
Cr$_2$O$_3$	<0·01	0·17	<0·01	0·02	0·33
FeO	1·74	2·22	2·03	2·38	4·13
MnO	<0·01	0·05	<0·01	0·05	0·08
MgO	22·59	22·52	22·22	22·87	21·23
CaO	7·38	7·55	8·16	7·07	7·41
Na$_2$O	5·95	5·18	5·37	5·53	5·35
K$_2$O	0·85	1·61	0·54	1·37	1·48
Sum	96·11	96·75	95·25	96·70	96·75
Mg-no.	95·86	94·75	95·12	94·48	90·16

(continued)

Clinopyroxene

	Dunite core	Wehrlite/clinopyroxenite rim			Metasomatic domain											(i.b.)
					(phl. d.)	(glimmerite veins)			(phlogopite–richterite clinopyroxenite veins)							
Sample:	K12	K2	K1	K1	drill cores											K26
n:	3	11	1	5	1	2	4	3	1	4	14	11	6	6	22	6
wt %																
SiO_2	53·95	53·91	54·44	52·28	53·60	54·70	52·71	51·35	54·73	54·57	54·28	53·95	53·70	53·50	52·02	50·86
TiO_2	0·18	0·17	0·04	0·27	0·28	0·08	0·40	0·74	0·29	0·24	0·17	0·27	0·33	0·39	0·56	0·75
Al_2O_3	0·94	0·79	0·11	1·48	0·52	0·01	1·49	2·23	0·11	0·05	0·42	0·55	0·60	0·62	1·86	2·52
Cr_2O_3	0·62	0·56	<0·01	0·03	0·03	<0·01	<0·01	<0·01	0·04	0·21	0·03	0·04	0·04	0·03	0·02	0·01
FeO	2·15	2·57	3·04	6·18	10·28	2·09	4·27	6·43	1·82	3·81	6·39	8·71	10·36	12·32	5·41	6·69
MnO	0·06	0·06	0·10	0·15	0·10	<0·01	<0·01	0·19	0·01	0·07	0·10	0·11	0·13	0·11	0·09	0·21
MgO	16·63	16·45	16·60	14·97	11·47	16·77	15·58	13·59	17·50	16·40	14·39	12·87	11·77	10·52	15·24	13·37
CaO	24·64	24·62	25·44	23·52	19·38	25·19	24·61	24·09	25·63	24·10	22·00	20·55	19·24	17·58	24·25	24·02
Na_2O	0·41	0·26	0·03	0·24	3·17	0·43	0·34	0·47	0·24	0·87	1·84	2·48	3·11	3·85	0·36	0·51
Sum	99·58	99·42	99·79	99·11	98·82	99·27	99·41	99·09	100·37	100·32	99·63	99·53	99·29	98·92	99·81	98·94
Mg-no.	95·21	92·17	91·12	85·09	82·97	95·99	91·64	83·97	94·91	92·50	90·29	85·56	82·95	78·87	90·18	84·63

Phlogopite

	Wehrlite/clinopyroxenite rim			Metasomatic domain												(i.b.)
				(phlogopite dunites)			(glimmerite veins)			(phlogopite–richterite clinopyroxenite veins)						
Sample:	K2	K1	K1	drill cores												K6	K26
n:	1	1	2	2	10	1	5	4	2	2	5	6	3	2	3	1	2
wt %																	
SiO_2	41·79	41·64	37·83	40·35	40·93	41·38	39·22	41·94	41·49	37·19	41·32	39·80	41·47	39·53	39·93	41·68	37·75
TiO_2	0·02	0·98	2·05	0·65	0·71	0·12	1·62	0·31	0·04	3·42	0·53	1·43	0·54	0·83	1·04	0·12	2·96
Al_2O_3	8·44	10·80	14·99	14·56	11·40	6·90	13·68	8·50	6·89	15·48	12·30	13·14	9·38	12·33	10·62	7·62	15·52
Cr_2O_3	<0·01	<0·01	0·08	1·58	0·12	<0·01	0·20	0·14	<0·01	0·02	0·06	0·07	0·01	<0·01	<0·01	0·00	0·01
FeO	7·42	5·26	10·16	3·09	5·24	9·63	5·03	7·26	9·39	10·63	4·59	5·40	6·75	8·90	12·46	9·04	8·64
MnO	<0·01	<0·01	0·05	<0·01	0·02	<0·01	0·01	0·03	0·00	0·05	0·02	0·02	0·02	0·10	0·12	<0·01	0·11
MgO	25·56	25·18	19·10	25·74	26·07	25·20	23·70	26·41	25·47	16·79	25·80	24·88	26·24	23·18	20·44	25·41	18·78
CaO	<0·01	<0·01	0·04	<0·01	<0·01	<0·01	<0·01	0·01	0·07	0·02	0·01	<0·01	0·01	0·01	0·03	<0·01	<0·01
Na_2O	0·94	0·89	0·68	0·65	1·20	0·72	0·76	0·75	0·77	0·40	1·35	1·04	0·76	0·63	0·55	0·75	0·78
K_2O	9·20	9·40	8·84	9·26	8·85	9·50	9·40	9·31	9·43	9·22	8·67	8·93	9·49	9·53	9·16	9·44	9·09
Sum	93·37	94·15	93·82	95·87	94·54	93·45	93·62	94·66	93·56	93·22	94·64	94·70	94·68	95·05	94·36	94·04	93·63
Mg-no.	85·99	89·50	77·01	93·69	89·87	82·34	89·38	86·63	82·86	73·79	90·93	89·15	87·40	82·28	74·52	83·36	79·48

(continued)

Table 2: Continued

Cr-spinel and Fe–Ti-oxides

	Main dunite core		Wehrlite/clinopyroxenite rim				Metasomatic domain										
							(phlogopite dunites)						(glimmerite veins)				
Sample:	K8	K12	K1	K1	K1	K1	drill cores											
n:	4	1	1	1	8	3	5	3	2	3	2	2	1	4	3	4	1	3
wt %																		
SiO$_2$	0·082	0·092	0·032	0·130	0·14	0·513	0·134	0·091	0·090	0·066	0·102	0·096	0·024	0·06	0·088	0·130	0·124	0·100
TiO$_2$	0·67	0·99	1·05	5·69	4·01	41·49	0·82	1·83	3·85	4·18	5·75	1·26	3·09	5·85	1·57	5·35	11·36	55·08
Al$_2$O$_3$	6·65	6·88	7·17	3·63	1·39	1·43	6·98	2·27	0fo·42	0·01	0·00	0·02	0·20	0·01	0·01	1·55	0·60	0·03
Cr$_2$O$_3$	53·24	44·42	47·94	21·26	0·72	0·02	44·99	41·79	27·80	11·03	3·61	1·30	42·66	5·70	1·22	0·03	0·01	0·00
FeO	28·22	39·67	35·18	56·92	84·71	39·05	35·28	45·28	59·92	75·41	81·76	88·55	45·07	79·24	88·65	81·90	78·48	32·52
MnO	0·47	0·63	0·00	0·00	0·32	1·82	0·00	0·08	0·74	0·00	0·00	0·24	0·00	0·00	0·00	0·69	0·96	2·19
MgO	10·42	6·71	6·04	4·96	0·94	5·24	7·48	4·53	3·57	2·99	1·50	1·35	4·66	2·48	1·35	1·64	1·48	8·51
NiO	0·084	0·061	0·145	0·155	0·055	0·020	0·102	0·104	0·235	0·242	0·235	0·344	0·192	0·211	0·213	0·026	0·000	0·007
Sum	99·84	99·45	97·56	92·74	92·28	89·59	95·78	95·98	96·62	93·93	92·97	93·15	95·89	93·56	93·10	91·32	93·00	98·45

Cr-spinel and Fe–Ti-oxides

Metasomatic domain
(phlogopite–richterite clinopyroxenite veins)

Sample:	drill cores												
n:	2	1	1	3	1	1	3	2	10	3	6	2	3
wt %													
SiO$_2$	0·147	0·024	0·098	0·098	0·045	0·075	0·086	0·108	0·08	0·088	0·090	0·358	0·130
TiO$_2$	0·53	2·06	1·01	1·93	4·64	4·92	5·23	4·89	1·33	0·96	5·73	25·14	56·87
Al$_2$O$_3$	5·67	2·79	5·57	5·36	0·03	0·04	0·12	0·02	0·03	0·01	0·02	0·08	0·00
Cr$_2$O$_3$	50·83	45·62	40·36	33·15	24·06	16·66	9·77	4·69	0·33	0·00	0·03	0·02	0·00
FeO	32·97	40·71	43·45	49·33	60·97	69·20	74·89	80·11	88·75	91·35	85·14	61·72	27·62
MnO	0·00	0·00	0·00	0·00	0·00	0·42	0·25	0·43	0·17	0·00	0·32	2·04	3·43
MgO	8·04	5·45	4·61	4·38	4·21	2·52	3·27	2·28	0·77	0·85	2·09	3·81	11·54
NiO	0·089	0·130	0·089	0·134	0·337	0·216	0·168	0·220	0·113	0·076	0·120	0·009	0·000
Sum	98·27	96·77	95·19	94·38	94·29	94·04	93·78	92·74	91·58	93·34	93·53	93·18	99·59

Analyses by electron microprobe analysis at 'Microsonde Sud' facility, Montpellier University, France. *n*, number of single analyses. Clinopyroxenite veins are phlogopite–richterite clinopyroxenites. phl. d., phlogopite dunite; i.b., intrusive bodies of phlogopite, apatite and Ti-magnetite clinopyroxenites.
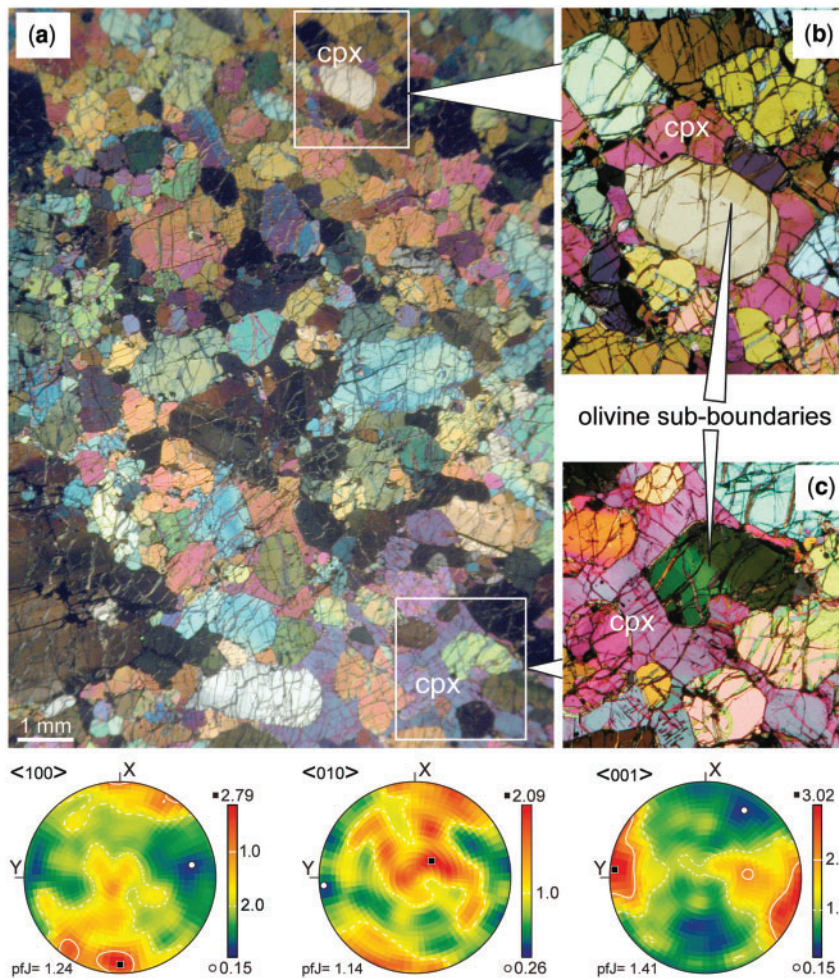
Fig. 4. Thin section and fabric of the K2 wehrlite (GPS: 57°35′27·6″N, 134°41′25·9″E, Fig. 2). Photomicrographs (a–c) and preferred orientation stereograms (bottom) represented in the thin-section plane, cut vertical and north–south in the geographical reference system. Lower hemisphere projection; electron back scattered diffraction (EBSD) measurements on 547 grain; pfJ index is representative of the fabric strength (Mainprice & Silver, 1993). Foliation is parallel to the reference plane; lineation deduced from the preferred orientation stereograms trends north–south.
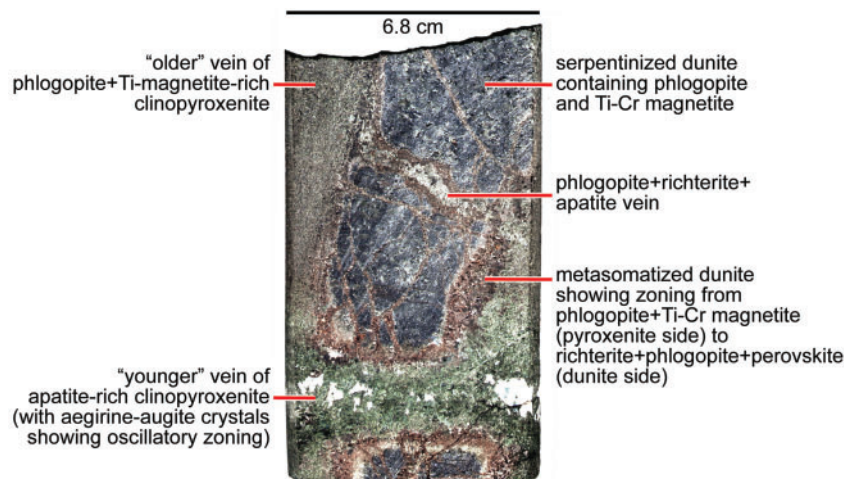

Fig. 5. Drill core sample (unspecified depth) from the metasomatic domain displaying typical K-metasomatic associations (sample courtesy of the Artel Amur mining company).

diffuse 'koswite' (i.e. phlogopite–amphibole–apatite–carbonate and Fe–Ti-oxide clinopyroxenite; Fig. 3b). This area also includes two major (>100 m) intrusions of phlogopite–apatite and Ti-magnetite clinopyroxenite (Sushkin, 1995). These intrusions were sampled by drilling to 800 m depth in the geographical centre of the ZUC (Orlova, 1992). Locally, the concentration of phlogopite-rich veins ('glimmerites') in the dunite has led to the formation of stockworks with an average composition of phlogopite-rich dunite. The dunites are brecciated and strongly metasomatized in the wall-rocks of the pyroxenite veins (Emelynenko *et al.*, 1989). The chromites are systematically coated by minor rutile (inward) and phlogopite (outward). They show compositional zoning from 'residual', chromium-rich cores to (Ti-)magnetite rims (Table 2). The largest crystals of Pt–Fe alloy are associated with these metasomatized rocks (Nekrasov *et al.*, 1994). The Artel Amur mining company provided us with open access to drill core samples from 100–150 m depth into the metasomatic domain, which allowed detailed observations of the mineralogy of the glimmerite and clinopyroxenite veins and their wall-rocks (Fig. 5; Table 1). The main secondary minerals include: (1) phlogopite showing a wide range of compositions (notably in Ti, Al, Cr and Fe), both between rock-types and within single, zoned crystals (Table 2); (2) different types of clinopyroxene, including light brown endiopside–diopside and green aegirine–augite, the latter being distinguished from the former by lower MgO (<15%) and CaO (<24%), higher Na_2O (>1%) contents (Table 2) and frequent chemical zoning; some crystals show oscillatory zoning marked by alternating bands of colourless augite (Mg-number = 89–92) and green aegirine–augite (Mg-number = 79–87); (3) amphibole of richterite composition (Table 2); (4) a variety of accessory minerals including Ca-carbonate, apatite, perovskite, titanite, rutile, Ti-magnetite, Mg-ilmenite and sulphides (Tables 1 and 2). This metasomatic mineral assemblage, occurring as a dense network of veinlets and veins in dunites, is strongly reminiscent of the MARID (mica–amphibole–rutile–ilmenite–diopside) xenolith suites from kimberlites (Dawson & Smith, 1977; Dawson, 1987).

Late dykes and peripheral intrusions

Several types of dykes cut the ultramafic rocks without any spatial concentration; they are, therefore, unrelated to the metasomatic domain: (1) fine-grained, magnetite-rich clinopyroxenites ('koswites'; Table 1); (2) amphibole-gabbros; (3) aegirine–albite–nepheline syenites (Fig. 3b). The koswites are somewhat akin to the magnetite-bearing rim clinopyroxenites and clinopyroxenite intrusions from the metasomatic domain with respect to their mineralogy, dominated by clinopyroxene and (Ti-)magnetite (± apatite and brown amphibole). However, they are distinguished by a much finer-grained, fluidal texture and the lack of patent metasomatism in their wall-rocks, suggesting that they represent hypovolcanic dykes intruded after substantial cooling of the ultramafic host.

The peripheral intrusions of diorite and monzodiorite and subordinate alkaline gabbros and granodiorites contain xenoliths of Kondyor pyroxenites (Fig. 3c), basement gneisses and marbles. The gabbros vary from coarse-grained, phlogopite-bearing to fine-grained, inclusion-rich rocks. The inclusions are of coarser-grained, darker gabbro, which suggests comagmatism.

Structures

General structure and kinematics

The ultramafic rocks have nearly vertical contacts with the Archaean basement (gneisses, quartzites and marbles), all around the massif. The surrounding hornfelsed sediments show a relatively steep (>60°), outward dipping layering, which rapidly flattens to horizontal away from the inner contact (Fig. 2). The late Proterozoic (Riphean) sedimentary cover—which is flat lying and virtually unmetamorphosed elsewhere—hence defines a 10–12 km diameter dome centred on the Kondyor ZUC. Structural reconstructions suggest that the top of the dunite–pyroxenite complex reached 0·7–0·5 km below the surface before being eroded to a depth of 1–1·8 km (Elianov & Moralev, 1972). Ductile, semi-brittle and brittle shear bands with down-dip lineations show that the ultramafic core has risen with respect to the country-rocks (Fig. 3d).

Olivine fabric

New foliation and lineation measurements in dunite obtained as part of this study are consistent with previous studies (Gurovich *et al.*, 1994; Zemlyanukhin & Prikhodko, 1997). The foliation generally dips inward, with a sharp change from >70° against the rim pyroxenites to 10–15° in the core (Fig. 2). The bulk synformal structure of the dunite foliation seems something of a paradox in the context of the Kondyor dome defined by the surrounding Riphean sediments. Mineral lineation trajectories are concentric (Fig. 2).

The textures and fabrics of 10 dunites and one wehrlite sample were analysed using the electron back scattered diffraction (EBSD) technique. In the absence of visual determination of penetrative structures in the dunites, thin sections were cut horizontally in the geographical reference system. Our results confirm, complement and strengthen the precision of the optically measured lattice preferred orientations (LPO) of olivine (Gurovich *et al.*, 1994; Zemlyanukhin & Prikhodko, 1997),

which define shallow-plunging, concentric flow-lines in the peridotites.

Four textural types, characterized by a distinct olivine LPO pattern were identified, from rim to core, as follows.

(1) High-temperature, coarse porphyroclastic (K28, Fig. 6), with large porphyroclasts (>1 mm) showing sharp (100) sub-boundaries. The texture contains variable proportions of polygonal grains (0·2–0·5 mm) attributed to subgrain rotation. The corresponding LPO has a strong maximum of the three crystallographic indexes. The classical relationships (010) close to foliation and [100] close to lineation imply that the slip system was [100](010). This texture suggests high-strain, solid-state flow by dislocation creep at an asthenospheric temperature (1100–1200°C; e.g. Nicolas & Poirier, 1976).

(2) Equigranular recrystallized (K19, Fig. 6), with polygonal neoblasts (0·2–0·5 mm) derived from the coarse porphyroclastic texture by increasing development of recrystallized grains (some porphyroclasts are still visible in this rock). Grain-size reduction by subgrain rotation marks larger amounts of strain and probably higher stress during flow by dislocation creep than the type (1) texture. The corresponding LPO is expressed by a stronger maximum of [100] compared with other axes.

(3) Tabular texture (K16, Fig. 6): coarse grains of tabular shape (3 mm × 1 mm), devoid of sub-boundaries, marked by a strong LPO with a strong maximum of [010]. Such a texture points to diffusion creep (Boullier & Nicolas, 1973).

(4) The last textural type characterizes pegmatitic dunites hosting phlogopite veins in the metasomatic zone. The LPO could not be measured because of the large grain size (5–10 mm). However, a strong preferred orientation of the sharp olivine (100) sub-boundaries indicates activation of the [100] (0kl) slip system, and large strain at high temperature. This substructure developed during or slightly after the active grain boundary migration responsible for the large grain size, and probably was triggered by fluids responsible for hydrofracturing and crystallization of phlogopite and associated minerals in veins.

The corresponding olivine LPOs (Fig. 6) are good, with the [001] *c*-axis as the strongest maximum. The slip system is the common [100] (010), with [100] close to lineation and (010) close to foliation; the marked [001] maximum probably results from large subgrain rotations, with [001] as the external rotation axis. The kinematics deduced from these fabrics indicates flow parallel to the mesoscopic lineation.

The wehrlite K2 exhibits a high-temperature porphyroclastic texture with a tendency to develop tabular olivine grains (Fig. 4a). Olivine grains show sharp (100) sub-boundaries, even in olivine inclusions in undeformed clinopyroxene poikiloblasts (Fig. 4b and c); this feature indicates that the rock developed from plastically deformed dunite, and that clinopyroxene crystallization post-dates the peridotite solid-state flow. The [001] axis makes the strongest maximum of the olivine LPO (Fig. 4). However, the slip system is the common [100] (010), with [100] close to lineation and (010) close to foliation; the [001] maximum probably results from large subgrain rotations, with [001] as external rotation axis. This olivine fabric is inherited from the dunite protolith, as the interstitial clinopyroxene is devoid of plastic deformation. This strain contrast precludes a cumulative origin for the wehrlite and supports a melt–rock reaction process. Preservation of the bulk fabric of the percolated dunite suggests that cpx crystallization has not disrupted the dunite solid framework, in support of progressive replacement of olivine by clinopyroxene via a reaction involving relatively small percolating melt fractions.

Dykes

Cross-cutting field relationships indicate that the usually steeply dipping clinopyroxene dykes are older than the syenitic, pegmatitic dykes (Fig. 3b). Structural measurements were difficult in the metasomatized magnetite-rich zone (unreliable, unstable compass direction), so that strike directions were specified by constructing directions from outcrop to far-distant geomorphological features. No clear pattern (e.g. radial vs concentric) exists for any of these sets (Fig. 7), although the veins and dykes visibly tend to dip predominantly towards the centre of the dunite body; phlogopite dykes dominantly dip to the east because they likely have been rotated with the metasomatic stockwork to which they pertain on the western limb of the generally synformal dunite (Fig. 2). Gently dipping pyroxenite veins are coarser along their upper, more mica- and apatite-rich margin where interstitial K-feldspar may occur. Nepheline-syenite pegmatites occur in all parts of the Kondyor ZUC. Dykes of fine-grained, sphene- and titanomagnetite-rich hornblendite cut all rock types of the ZUC (Orlova, 1992).

GEOCHEMISTRY
Analytical procedures

After crushing, sample aliquots were pulverized in a Pulverisette® agate mortar for solution analysis. Major elements, Cr and Zn in whole-rocks were mostly analyzed by inductively coupled plasma-atomic emission spectrometry (ICP-AES) at CRPG (Nancy, France)
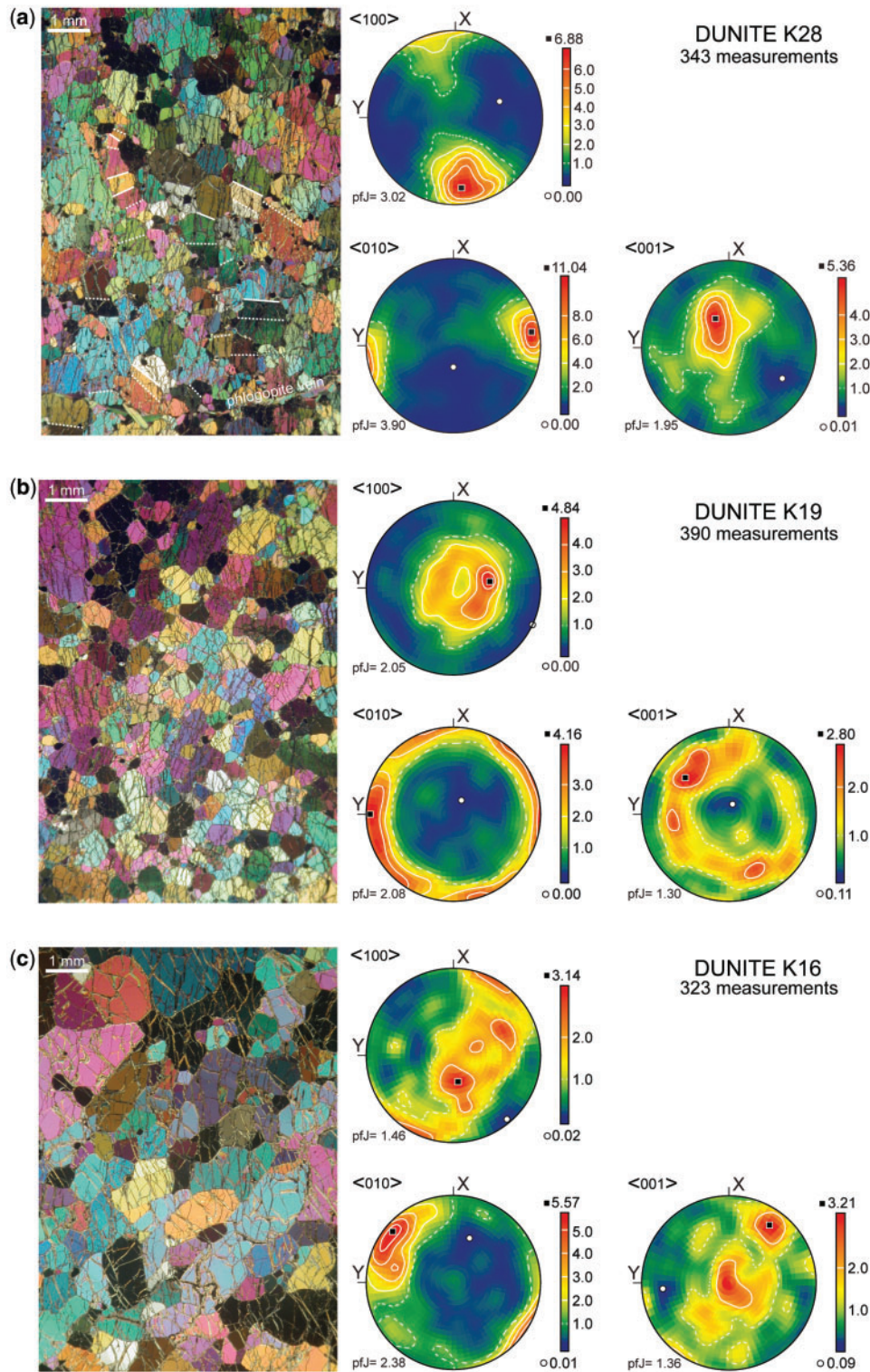
Fig. 6. Textures (left) and olivine fabrics (stereograms) in dunites representative of the three domains (Fig. 2). Same reference frame as in Fig. 4 (i.e. thin section cut in north–south vertical plane). (a) K28 (GPS: 57°34′44·7″N, 134°38′22·9″E, Fig. 2): high-*T* porphyroclastic texture: trace of foliation and lineation are north–south in the reference frame; dotted lines indicate sub-boundaries visible on the photomicrograph; continuous lines are grain boundaries that evolved by subgrain rotation (Nicolas & Poirier, 1976). (b) K19 (GPS: 57°34′53·1″N, 134°36′42·3E, Fig. 2): recrystallized texture: foliation and lineation are respectively parallel and perpendicular to the reference plane; sub-boundaries are rarely visible in this plane. (c) K16 (GPS: 57°33′18·6″N, 134°40′07·1″E, Fig. 2): tabular texture: trace of foliation and lineation trending NE–SW in the reference frame.
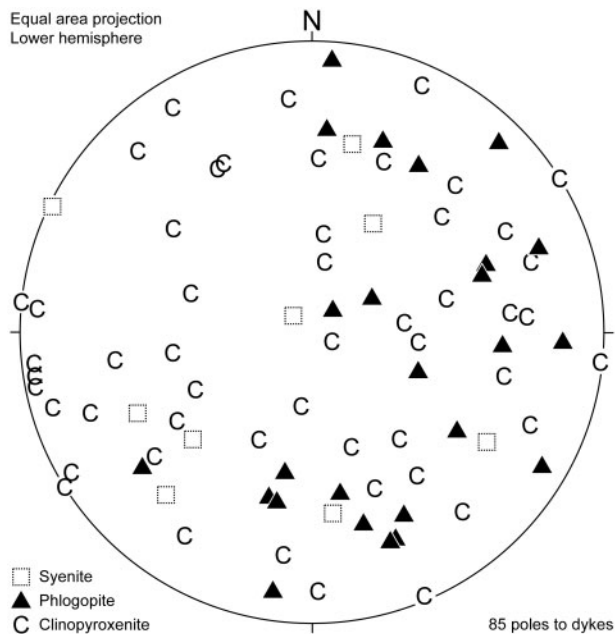
Fig. 7. Stereonet projection of dyke orientations (equal area, lower hemisphere).

following standard procedures. Exceptions include major elements and Cr in samples 8385, 8266, 8235, 8375, 8253, 8258, 8486, 8491 and 8216 (rim gabbros, intrusive phlogopite, apatite and Ti-magnetite clinopyroxenites, amphibole-gabbro and syenite dykes), which were analyzed by wet chemical methods at the Ekaterinburg Institute of Geology and Geochemistry (Russia), and TiO_2 in dunites, which was analyzed by ICP-MS. Minor and trace elements (Sc, Ti, Co, Ni, Cu, Rb, Sr, Y, Zr, Nb, Ba, REE, Hf, Ta, Pb, Th and U) in whole-rocks were analyzed by solution ICP-MS. We used for sample dissolution the $HF–HClO_4–HNO_3$ digestion procedure described by Ionov et al. (1992) and the analyses were obtained using a VG-PQ2 quadrupole instrument at Géosciences Montpellier, France (AETE Regional ICP-MS Facility). Concentrations were determined by external calibration for most elements except Nb and Ta, which were calibrated by using Zr and Hf, respectively, as internal standards. This technique is an adaptation to ICP-MS analysis of the method described by Jochum et al. (1990) for the determination of Nb by spark-source mass spectrometry. This method avoids memory effects caused by the introduction of concentrated Nb–Ta solutions into the instrument. Detection limits obtained by long-term analyses of chemical blanks have been given by Ionov et al. (1992), Godard et al. (2000) and Garrido et al. (2000). Whole-rock data are reported in Table 3.

Dunite core

The dunites have extremely refractory compositions, with Al_2O_3 contents mostly < 0·2 wt.% (Table 3). The dunite body is zoned with respect to Mg-number (Fig. 8) and Ni; the central part (>200 m from the pyroxenite rim) shows a compositional 'plateau' at Mg-number = 88–91 and Ni 1280–1520 ppm, whereas the outer part is distinguished by lower Mg-number (85–88) and Ni contents (990–1230 ppm). Other major and trace elements do not show significant variations at the massif scale. The significant variability of Cr (2200–5130 ppm) reflects the heterogeneous distribution of Cr-spinel at the sample scale.

The dunites are strongly depleted in heavy rare earth elements (HREE) and other moderately incompatible elements (e.g. Ti; Table 3) relative to primitive mantle values (PM), with HREE contents mostly in the range 0·01–0·1 × PM (Fig. 9). However, they are selectively enriched in light REE (LREE) and highly incompatible elements (HIE) relative to HREE, with Rb, Ba and U in the range (0·1–1) × PM. The high field strength elements (HFSE: Nb, Ta, Zr, Hf) show negative anomalies relative to neighbouring elements (Fig. 9). Selective HIE enrichment associated with negative HFSE anomalies is a common feature in refractory mantle rocks from the subcontinental lithosphere (Fig. 9; Bedini et al., 1997). The trace-element distribution in dunites is strongly reminiscent of that measured in Kondyor pyroxenites and igneous dykes, as well as in Aldan Shield lamproites (Davies et al., 2006; Fig. 10), but the dunites are distinguished from these rocks by higher La/Yb values at a given La content (Fig. 11).

Rim pyroxenites

The wehrlites and clinopyroxenites rimming the Kondyor peridotites show a wide range of compositions, with a gradual and irregular variation from the inner, wehrlitic zone, transitional to cpx-bearing dunites toward the outer, oxide-bearing cumulate clinopyroxenites, which are transitional to the peripheral gabbros and syenites (Table 3; Fig. 8). The wehrlites overlap the outermost dunites with respect to Mg-number (85–87) and resemble the latter in terms of most of their major- and trace-element characteristics. They are nevertheless distinguished from the dunites by much higher Ca concentrations (CaO 7·7–11·3%, compared with 0·3–0·6%), significantly lower Ni and Co contents (Ni 460–590 ppm) and slightly more enriched Al, Ti, Sc and incompatible trace elements. Conversely, the outermost, oxide-bearing cumulate clinopyroxenites have low Mg-number values (45–47), within the variation range of the adjacent ring gabbros and syenites (32–64). In addition to Fe, the oxide-bearing clinopyroxenites are enriched in Ti but do not otherwise differ markedly from the other rim clinopyroxenites. Compared with the

Table 3: Whole-rock major- and trace-element compositions of Kondyor ultramafic rocks and related intrusive rocks

Main dunite core

Sample:	8323	8305	8304	K16	8308	8201	8192	8388	8319	8198	8398	K19	8408	K23	8226	8409	8403
wt %																	
SiO_2	39·74	39·60	39·62	39·09	39·43	39·37	39·07	39·57	39·34	38·82	38·98	39·47	40·02	39·71	38·97	39·54	39·44
TiO_2	0·013	0·011	0·011	0·009	0·013	0·018	0·015	0·028	0·015	0·015	0·019	0·009	0·033	0·016	0·012	0·019	0·022
Al_2O_3	0·10	0·10	0·07	<0·05	0·11	0·17	0·08	0·16	0·19	0·14	0·18	<0·05	0·21	0·12	0·10	0·09	0·09
Fe_2O_3	9·91	9·84	10·04	9·34	10·38	10·26	10·51	10·46	11·51	11·16	11·53	11·15	12·82	11·74	12·56	14·19	14·91
MnO	0·17	0·17	0·17	0·16	0·17	0·17	0·18	0·17	0·19	0·20	0·19	0·19	0·21	0·18	0·19	0·22	0·24
MgO	47·54	47·19	47·67	47·93	47·36	46·27	46·61	45·90	45·88	44·48	45·88	46·70	46·50	46·78	45·30	46·74	45·48
CaO	0·30	0·29	0·31	0·42	0·27	0·32	0·47	0·67	0·45	0·33	0·34	0·41	0·62	0·54	0·56	0·47	0·34
Na_2O	<0·02	<0·02	<0·02	<0·02	<0·02	<0·02	<0·02	<0·02	0·02	0·02	<0·02	<0·02	0·03	<0·02	<0·02	<0·02	<0·02
K_2O	<0·02	0·03	<0·02	<0·02	<0·02	<0·02	<0·02	<0·02	0·03	<0·02	<0·02	<0·02	<0·02	<0·02	<0·02	<0·02	<0·02
P_2O_5	0·06	0·08	0·06	0·07	0·07	0·08	0·07	0·08	0·09	0·09	0·08	0·07	0·09	0·09	0·08	0·09	0·08
LOI	3·20	4·00	2·98	3·02	3·51	4·60	3·97	4·46	3·29	5·72	4·36	1·99	1·17	0·96	3·24	0·48	1·34
Sum	101·03	101·31	100·93	100·04	101·31	101·26	100·97	101·50	101·01	100·98	101·56	99·99	101·70	100·14	101·01	101·84	101·94
Mg-no.	90·5	90·5	90·4	90·1	90·0	89·9	89·8	89·7	88·8	88·8	88·7	88·2	87·8	87·7	87·7	86·7	85·8
ppm																	
Sc	4·70	4·44	4·49	3·71	4·68	4·13	4·79	5·04	5·00	4·19	4·81	4·12	6·28	5·27	5·09	5·35	5·45
Ti	76	64	63	56	79	107	87	169	92	90	116	51	199	98	70	111	133
Cr	3540	2260	2190	n.a.	3590	3630	3170	5130	4480	2820	4590	n.a.	2770	n.a.	2990	2740	2690
Co	142	141	141	133	140	133	127	140	149	147	135	160	162	166	144	159	164
Ni	1622	1534	1558	1279	1515	1437	1362	1580	1357	1401	1462	1134	1135	1230	991	1110	1079
Cu	6·5	8·2	13·7	1·2	11·6	15·4	9·1	19·7	6·1	9·9	23·9	4·03	9·9	5·7	18·7	22·0	16·3
Zn	57	57	54	n.a.	56	58	57	58	68	65	62	n.a.	79	n.a.	60	68	79
Rb	0·081	0·071	0·087	0·018	0·072	0·87	0·181	0·263	0·258	0·204	0·184	0·083	0·60	0·044	0·089	0·084	0·146
Sr	0·86	3·61	0·92	0·31	0·73	1·96	1·21	2·12	9·3	9·7	1·59	0·47	7·9	1·08	1·53	1·09	1·06
Y	0·066	0·090	0·076	0·061	0·065	0·097	0·091	0·209	0·063	0·159	0·144	0·056	0·36	0·079	0·074	0·090	0·116
Zr	0·103	0·206	0·137	0·036	0·068	0·188	0·139	0·314	0·234	0·55	0·307	0·045	0·65	0·076	0·105	0·202	0·157
Nb	0·018	0·073	0·023	0·011	0·012	0·035	0·021	0·024	0·022	0·109	0·031	0·037	0·080	0·027	0·025	0·030	0·025
Cs	0·0059	0·0030	0·0032	0·0007	0·0020	0·011	0·0036	0·0078	0·0028	0·0083	0·0064	0·024	0·022	0·017	0·0035	0·0030	0·0030
Ba	1·73	1·67	1·24	0·145	1·25	6·1	1·48	3·05	3·52	6·0	2·78	0·78	5·4	1·10	1·38	0·67	2·16
La	0·025	0·063	0·021	0·0025	0·0120	0·085	0·033	0·078	0·093	0·316	0·050	n.a.	0·297	0·026	0·037	0·035	0·045
Ce	0·045	0·110	0·043	0·0038	0·024	0·131	0·056	0·208	0·132	0·63	0·113	0·022	0·67	0·042	0·068	0·077	0·116
Pr	0·0064	0·0125	0·0059	0·00086	0·0038	0·0188	0·0077	0·0301	0·0131	0·070	0·0178	0·0044	0·089	0·0079	0·0097	0·0112	0·0151
Nd	0·028	0·053	0·027	0·0027	0·0143	0·081	0·031	0·160	0·049	0·287	0·071	0·021	0·389	0·035	0·044	0·045	0·073
Sm	0·0093	0·0116	0·0073	0·0021	0·0055	0·0195	0·0105	0·047	0·0120	0·052	0·020	0·0097	0·092	0·0110	0·0110	0·0123	0·0186
Eu	0·0026	0·0043	0·0024	0·00086	0·0019	0·0057	0·0033	0·0138	0·0036	0·0144	0·0070	0·0015	0·025	0·0027	0·0036	0·0044	0·0058
Gd	0·0080	0·0136	0·0094	0·0064	0·0072	0·0190	0·0129	0·052	0·0098	0·042	0·022	0·0101	0·087	0·0152	0·0124	0·0150	0·0200
Tb	0·0014	n.a.	n.a.	0·0011	0·0013	0·0027	0·0020	0·0075	0·0017	0·0058	0·0037	0·0017	0·0126	0·0019	0·0020	0·0022	0·0030
Dy	0·0111	0·0159	0·0135	0·0095	0·0102	0·0184	0·0161	0·044	0·0119	0·033	0·024	0·0085	0·074	0·0135	0·0147	0·0160	0·020
Ho	0·0030	0·0037	0·0031	0·0023	0·0027	0·0046	0·0036	0·0088	0·0031	0·0067	0·0061	0·0025	0·0155	0·0036	0·0031	0·0040	0·0050
Er	0·0119	0·0118	0·0115	0·0101	0·0111	0·0150	0·0136	0·026	0·0117	0·024	0·0189	0·0090	0·045	0·0136	0·0107	0·0132	0·0163
Tm	0·0022	n.a.	n.a.	0·0020	0·0020	0·0026	0·0023	n.a.	0·0022	0·0038	0·0035	0·0024	0·0064	0·0026	0·0017	n.a.	0·0032
Yb	0·0175	0·0193	0·0178	0·0159	0·0185	0·0179	0·021	0·028	0·0157	0·027	0·024	0·0160	0·043	0·0170	0·0135	0·0197	0·028
Lu	0·0037	0·0045	0·0038	0·0037	0·0040	0·0039	0·0045	0·0054	0·0036	0·0053	0·0052	0·0041	0·0080	0·0039	0·0027	0·0041	0·0062
Hf	0·0049	0·0054	0·0041	0·0020	0·0027	0·0073	0·0062	0·0128	0·0097	0·0159	0·0093	0·0026	0·025	0·0045	0·0035	0·0060	0·0062
Ta	<0·0005	0·0024	0·00084	0·00081	0·00064	<0·0005	0·00123	0·00154	0·00108	0·0036	<0·0005	0·00185	0·0044	0·00166	0·00093	0·00182	0·00120
Pb	0·14	0·24	0·17	0·01	0·27	0·18	0·24	0·43	0·57	0·22	0·53	0·10	0·26	0·03	0·24	0·19	0·32
Th	0·0035	0·0110	0·0078	0·0018	0·0028	0·0073	0·0058	0·0078	0·0028	0·042	0·0098	0·0016	0·040	0·0050	0·0079	0·0073	0·0063
U	0·0039	0·0051	0·0037	0·0010	0·0018	0·0066	0·0029	0·0056	0·0019	0·0127	0·0048	0·0086	0·0144	0·032	0·0046	0·0037	0·0025

(continued)

Table 3: Continued

Pyroxenite rim and gabbro or syenite intrusives

	wehrlites			clinopyroxenites								gabbros			neph. syenite
Sample:	K2	K3	K4	K35	8443	8302	8276	K18	8439	K1	K37	8385	8266	8235	K21
wt %															
SiO_2	42·91	44·90	44·87	51·47	50·53	51·04	48·49	49·68	46·25	39·77	39·38	47·91	39·71	44·58	52·20
TiO_2	0·07	0·10	0·10	0·25	0·28	0·21	0·29	0·32	0·67	1·72	2·00	0·99	1·97	1·46	1·42
Al_2O_3	0·32	0·43	0·46	1·04	1·51	0·88	1·56	1·49	1·76	1·93	2·72	8·13	7·02	7·56	16·23
Fe_2O_3	10·05	9·32	10·02	5·63	6·37	6·86	10·54	10·47	14·58	25·05	25·59	11·88	22·44	20·93	10·61
MnO	0·17	0·15	0·16	0·10	0·11	0·12	0·19	0·18	0·19	0·19	0·24	0·19	0·28	0·21	0·29
MgO	37·76	33·69	32·09	18·31	18·37	19·42	20·99	18·00	16·45	12·61	11·71	10·75	10·13	8·70	2·81
CaO	7·69	10·69	11·31	22·05	20·85	21·13	17·70	19·90	19·46	18·14	17·88	14·93	16·77	14·70	6·61
Na_2O	<0·02	<0·02	0·05	0·22	0·31	0·19	0·20	0·29	0·23	0·08	0·26	1·25	0·68	1·15	3·65
K_2O	<0·02	<0·02	<0·02	<0·02	0·19	<0·02	<0·02	<0·02	<0·02	<0·02	0·06	2·47	<0·02	0·66	5·54
P_2O_5	<0·02	<0·02	<0·02	0·08	0·09	0·04	0·05	0·11	0·05	<0·02	0·20	0·46	0·92	0·11	0·48
LOI	0·92	0·88	0·71	0·84	1·29	-0·07	1·01	0·03	0·77	-0·49	-0·17	1·37	1·00	0·13	0·50
Sum	99·89	100·16	99·77	99·99	99·90	99·82	101·02	100·47	100·41	99·00	99·87	100·33	100·92	100·19	100·34
Mg-no.	87·0	86·6	85·1	85·3	85·1	84·9	79·8	75·4	69·1	47·3	44·9	64·2	47·2	45·2	32·1
ppm															
Sc	16·8	20·8	27·7	3·50	59	63	77	81	78	84	63	52	61	62	18·3
Ti	373	422	579	63	1900	1510	2030	1630	4540	6719	n.a.	7018	11244	10832	10835
Cr	2562	n.a.	n.a.	1818	2470	1450	1500	n.a.	615	n.a.	n.a.	620	70	70	n.a.
Co	101	81	99	146	48·5	54	74	84	82	103	47·7	64	77	70	28·2
Ni	586	459	529	1542	179	196	241	154	162	152	166	168	131	134	99
Cu	5·1	4·4	6·7	2·7	23·8	6·5	6·9	7·9	14·7	37·4	6·9	145	73	331	132
Zn	54	n.a.	n.a.	29·4	44·6	53	71	n.a.	76	n.a.	n.a.	86	156	123	n.a.
Rb	0·154	0·157	0·107	0·396	8·9	0·127	0·70	1·52	1·39	0·324	4·96	70	1·37	26·5	69
Sr	22·2	30·9	31·4	69	108	78	58	76	116	56	100	423	445	232	3582
Y	0·54	0·67	0·68	2·21	3·50	3·12	6·5	5·3	4·75	4·77	7·6	12·1	23·5	16·0	28·9
Zr	0·67	0·87	1·02	3·47	6·4	2·47	7·6	13·0	7·4	11·1	17·9	32·4	33·6	36·7	183
Nb	0·041	0·049	0·028	0·078	0·205	0·039	0·076	0·064	0·078	0·230	0·70	3·03	0·86	1·67	19·6
Cs	0·0064	0·0090	0·0112	0·021	0·219	0·0059	0·022	0·054	0·042	0·023	0·106	1·02	0·037	0·385	0·049
Ba	0·49	0·63	0·48	2·03	36·4	1·98	6·6	9·3	14·8	5·7	34·2	551	43·6	161	1132
La	0·126	0·153	0·174	0·66	1·62	0·59	0·98	1·60	1·17	0·93	2·41	8·6	12·9	6·8	32·5
Ce	0·456	0·56	0·63	2·43	4·36	1·97	3·50	5·7	3·78	3·61	8·2	20·4	33·5	17·8	77
Pr	0·089	0·110	0·120	0·46	0·70	0·41	0·72	0·99	0·74	0·72	1·48	2·87	5·1	2·66	9·6
Nd	0·55	0·67	0·75	2·79	3·58	2·36	4·29	5·6	4·28	4·50	8·8	13·6	25·7	13·1	42·3
Sm	0·165	0·208	0·237	0·85	0·94	0·73	1·34	1·63	1·30	1·42	2·65	3·25	6·3	3·46	8·3
Eu	0·055	0·067	0·079	0·285	0·290	0·236	0·420	0·52	0·412	0·456	0·79	0·95	1·82	0·98	2·56
Gd	0·180	0·223	0·255	0·98	0·95	0·80	1·49	1·87	1·38	1·61	3·06	3·30	6·5	3·71	7·3
Tb	0·0246	0·0306	0·036	0·140	0·135	0·116	0·225	0·275	0·193	0·230	0·448	0·442	0·89	0·56	1·07
Dy	0·143	0·175	0·203	0·82	0·79	0·68	1·38	1·70	1·09	1·37	2·67	2·56	5·1	3·41	6·8
Ho	0·0255	0·0306	0·0361	0·145	0·145	0·128	0·270	0·309	0·199	0·243	0·481	0·487	0·97	0·67	1·26
Er	0·067	0·077	0·087	0·344	0·371	0·317	0·70	0·76	0·476	0·58	1·15	1·26	2·46	1·76	3·52
Tm	0·0094	0·0102	0·0116	0·0449	0·0483	0·0405	0·093	0·105	0·061	0·075	0·151	0·168	0·317	0·243	0·495
Yb	0·053	0·062	0·071	0·252	0·289	0·246	0·55	0·59	0·355	0·419	0·84	1·03	1·81	1·49	2·99
Lu	0·0097	0·0105	0·0122	0·040	0·044	0·038	0·087	0·093	0·057	0·065	0·132	0·158	0·270	0·229	0·438
Hf	0·0218	0·0279	0·0355	0·150	0·239	0·114	0·338	0·418	0·350	0·355	0·68	1·13	1·42	1·35	5·9
Ta	0·00133	0·00145	0·00134	0·0024	0·0122	0·00120	0·0037	0·0029	0·0054	0·0077	0·031	0·186	0·068	0·104	1·14
Pb	0·04	0·05	0·10	0·09	1·72	0·17	0·44	0·14	0·60	0·06	0·34	1·70	1·60	1·40	4·56
Th	0·0056	0·0083	0·0124	0·0126	0·0717	0·0068	0·0311	0·0375	0·0353	0·0082	0·085	0·356	0·373	0·225	1·25
U	0·00286	0·0040	0·0068	0·0064	0·0260	0·0027	0·0100	0·0125	0·0098	0·0050	0·0326	0·111	0·112	0·058	0·308

(continued)

Table 3: Continued

	Metasomatic domain									
	dunite	phlogopite dunites								
Sample:	K27	142b	141	K28	142a	141d	143	120d	121d	K29
wt %										
SiO$_2$	38·69	40·33	40·30	39·70	40·55	40·20	40·43	40·20	39·83	38·59
TiO$_2$	0·009	0·008	0·004	0·020	0·009	0·036	0·007	0·05	0·07	0·09
Al$_2$O$_3$	0·10	0·21	0·22	0·34	<0·05	0·17	<0·05	0·31	0·26	0·79
Fe$_2$O$_3$	9·11	9·57	9·60	9·54	9·96	10·15	10·64	10·82	11·36	11·00
MnO	0·15	0·17	0·17	0·16	0·18	0·20	0·19	0·20	0·23	0·21
MgO	47·24	48·35	48·18	47·74	49·56	48·36	48·36	47·87	46·87	44·19
CaO	0·42	0·37	0·49	0·43	0·35	0·39	0·50	0·57	0·72	0·77
Na$_2$O	<0·02	0·09	0·06	<0·02	<0·02	<0·02	<0·02	<0·02	0·06	0·05
K$_2$O	<0·02	<0·02	<0·02	0·08	<0·02	<0·02	<0·02	0·09	0·11	0·26
P$_2$O$_5$	0·09	0·08	0·08	0·08	0·09	0·10	0·08	0·10	0·11	0·10
LOI	4·31	0·75	0·85	2·07	-0·36	0·44	-0·35	-0·27	0·24	3·45
Sum	100·12	99·93	99·95	100·16	100·34	100·05	99·86	99·94	99·86	99·50
Mg-no.	90·2	90·0	89·9	89·9	89·9	89·5	89·0	88·7	88·0	87·7
ppm										
Sc	4·26	3·27	7·4	4·38	3·75	3·55	4·73	4·18	4·19	4·36
Ti	52	49	25·2	122	51	217	44·9	313	358	552
Cr	n.a.	n.a.	n.a.	n.a.	n.a.	n.a.	n.a.	n.a.	1803	n.a.
Co	134	124	118	153	139	131	155	133	121	138
Ni	1543	1280	2394	1552	1394	1225	1240	1198	937	1142
Cu	3·54	2·38	7·3	6·2	3·58	4·76	2·11	12·5	17·4	21·0
Zn	n.a.	n.a.	n.a.	n.a.	n.a.	n.a.	n.a.	n.a.	82	n.a.
Rb	0·0180	1·15	0·57	4·23	0·047	4·02	0·033	5·8	5·9	9·6
Sr	0·69	18·8	21·9	11·7	5·6	16·1	11·2	22·1	45·1	18·3
Y	0·047	0·226	0·233	0·397	0·091	0·241	0·111	0·336	0·331	0·66
Zr	0·067	2·67	1·43	0·82	0·144	0·80	0·354	1·63	2·23	1·94
Nb	0·050	0·190	0·172	0·160	0·065	0·049	0·111	0·144	0·154	0·38
Cs	0·0029	0·021	0·0113	0·044	0·0015	0·044	0·0010	0·050	0·072	0·089
Ba	0·09	4·28	5·9	8·9	0·33	8·8	0·36	17·9	8·1	30·3
La	0·235	0·354	0·475	0·167	0·077	0·244	0·101	0·230	0·259	0·257
Ce	0·027	0·64	0·82	0·48	0·142	0·46	0·183	0·56	0·49	0·82
Pr	0·0047	0·071	0·093	0·072	0·0193	0·056	0·023	0·081	0·063	0·139
Nd	0·0167	0·284	0·36	0·33	0·073	0·190	0·105	0·40	0·291	0·76
Sm	0·0081	0·051	0·073	0·072	0·0198	0·041	0·029	0·089	0·064	0·174
Eu	0·00219	0·0172	0·0224	0·0256	0·0066	0·0130	0·0084	0·0261	0·0203	0·055
Gd	0·0076	0·048	0·065	0·067	0·0200	0·042	0·0261	0·084	0·066	0·177
Tb	0·00124	0·0077	0·0092	0·0118	0·0026	0·0065	0·00429	0·0115	0·0094	0·0255
Dy	0·0078	0·046	0·057	0·076	0·0187	0·046	0·027	0·072	0·062	0·158
Ho	0·0024	0·0097	0·0126	0·0168	0·0045	0·0099	0·0053	0·0141	0·0134	0·0310
Er	0·0123	0·041	0·0395	0·051	0·0183	0·0309	0·0207	0·043	0·046	0·088
Tm	0·0025	0·0059	0·0056	0·0093	0·0031	0·0054	0·0034	0·0068	0·0069	0·0136
Yb	0·0169	0·0399	0·0402	0·063	0·0209	0·0391	0·0261	0·0433	0·050	0·090
Lu	0·0040	0·0077	0·0074	0·0124	0·0053	0·0076	0·0057	0·0080	0·0097	0·0173
Hf	0·0051	0·068	0·046	0·0320	0·0065	0·0222	0·0094	0·045	0·061	0·084
Ta	0·00145	0·0130	0·0055	0·0065	0·00213	0·00199	0·0038	0·0053	0·0053	0·0170
Pb	0·01	0·34	1·20	<0·01	0·04	0·02	0·10	0·07	0·10	0·06
Th	0·0044	0·067	0·0402	0·0024	0·0093	0·0036	0·0101	0·0074	0·0053	0·0083
U	0·0021	0·0265	0·0163	0·00163	0·0047	0·00117	0·0059	0·0028	0·0030	0·0028

(continued)

Table 3: Continued

	Metasomatic domain							Late dykes				
	phlogopite and richterite clinopyroxenites (veins)			phlogopite, apatite and Ti-magnetite clinopyroxenites (intrusive bodies)				koswites		amphibole gabbros		nepheline syenite
Sample:	121p	120p	K6	8375	8253	K26	8258	K9	K7	8486	8491	8216
wt %												
SiO$_2$	39·39	37·74	30·77	36·25	35·44	35·82	34·35	37·02	33·40	42·78	45·27	64·75
TiO$_2$	1·99	2·16	3·54	2·06	2·04	2·33	1·60	2·45	3·07	1·96	1·67	0·34
Al$_2$O$_3$	4·73	3·78	2·77	9·92	9·62	4·10	4·04	8·62	3·04	10·97	7·04	17·32
Fe$_2$O$_3$	21·30	21·82	32·48	20·01	21·42	22·55	30·22	20·20	29·88	20·94	13·07	5·23
MnO	0·16	0·18	0·42	0·25	0·22	0·28	0·42	0·42	0·47	0·42	0·14	0·03
MgO	14·30	14·20	9·54	13·01	13·05	11·91	12·00	9·70	9·54	1·91	12·99	0·70
CaO	14·33	16·03	17·93	10·60	12·13	18·40	16·25	16·98	18·51	14·72	11·83	0·85
Na$_2$O	0·56	0·69	0·28	0·67	0·64	0·45	0·47	1·48	0·33	2·55	3·93	9·85
K$_2$O	2·36	1·61	<0·02	4·34	3·00	1·16	0·03	0·86	<0·02	0·69	0·03	0·30
P$_2$O$_5$	0·13	0·99	1·96	2·81	2·04	2·30	0·88	1·53	1·56	1·53	0·65	0·04
LOI	0·61	0·46	−0·92	1·24	1·37	0·34	1·21	0·24	-0·48	2·06	3·83	0·42
Sum	99·86	99·66	98·77	101·16	100·97	99·64	101·47	99·50	99·32	100·53	100·45	99·83
Mg-no.	54·5	53·7	34·4	66·0	54·5	48·5	43·6	46·1	36·3	14·9	70·7	20·7
ppm												
Sc	81	82	56	n.a.	n.a.	71	n.a.	53	43·8	n.a.	n.a.	n.a.
Ti	10798	12008	19295	n.a.	n.a.	11681	n.a.	13530	16311	n.a.	n.a.	n.a.
Cr	n.a.	n.a.	n.a.	20	20	n.a.	70	n.a.	n.a.	410	50	50
Co	80	79	89	80	90	71	120	65	80	n.a.	n.a.	n.a.
Ni	217	244	198	n.a.	n.a.	139	n.a.	158	155	n.a.	n.a.	n.a.
Cu	68	240	114	n.a.	n.a.	907	n.a.	376	212	n.a.	n.a.	n.a.
Zn	n.a.	n.a.	n.a.	n.a.	n.a.	137	n.a.	n.a.	n.a.	n.a.	n.a.	n.a.
Rb	80	51	0·70	169	143	43·6	1·15	4·45	0·179	4·51	0·443	8·9
Sr	168	763	443	446	317	457	399	1098	442	1151	2813	825
Y	4·27	10·9	28·0	20·2	14·7	20·3	20·4	33·8	26·2	33·1	13·8	0·99
Zr	19·2	28·2	57	14·2	16·1	25·6	63	143	59	106	137	53
Nb	1·95	2·83	0·66	1·33	1·16	0·68	0·47	8·0	0·64	8·1	17·3	3·75
Cs	0·68	0·49	0·065	0·97	0·97	0·300	0·014	0·046	0·021	0·082	0·019	0·097
Ba	252	226	9·7	881	681	228	9·5	177	9·4	175	24	125
La	3·55	29·9	36·1	27·4	16·1	26·3	19·1	39·3	33·5	39·6	59	3·19
Ce	8·7	58	96	69	41·6	68	53	103	85	93	132	6·0
Pr	1·35	7·0	13·6	10·2	6·3	9·8	8·2	14·0	11·3	12·6	16·9	0·63
Nd	7·3	32·6	68	50·0	31·4	51	41·1	69	59	57	67	2·22
Sm	1·76	6·4	14·3	10·0	6·7	10·5	8·9	14·4	13·0	11·4	11·0	0·377
Eu	0·54	1·79	4·04	2·84	1·93	3·03	2·66	4·29	3·59	3·47	3·41	0·115
Gd	1·73	5·2	12·3	9·2	6·1	9·5	8·2	12·2	10·1	10·5	7·9	0·309
Tb	0·221	0·63	1·49	1·05	0·72	1·12	1·04	1·63	1·34	1·39	0·93	0·0393
Dy	1·17	3·41	8·2	5·3	3·77	6·0	5·6	9·3	7·9	7·8	4·49	0·219
Ho	0·196	0·53	1·32	0·88	0·65	0·94	0·95	1·55	1·21	1·44	0·67	0·0390
Er	0·50	1·17	2·96	1·90	1·44	2·16	2·19	3·86	2·69	3·49	1·40	0·102
Tm	0·060	0·136	0·338	0·205	0·159	0·242	0·260	0·487	0·347	0·447	0·158	0·0151
Yb	0·326	0·72	1·81	1·04	0·86	1·25	1·53	2·83	1·99	2·62	0·98	0·117
Lu	0·051	0·105	0·263	0·144	0·123	0·177	0·256	0·428	0·272	0·406	0·171	0·0254
Hf	0·87	1·53	2·80	0·67	0·76	1·22	3·35	5·7	2·99	4·04	5·6	1·89
Ta	0·054	0·087	0·066	0·092	0·083	0·0490	0·061	0·479	0·074	0·59	2·35	0·158
Pb	0·20	0·79	0·22	1·68	2·24	0·49	1·51	1·14	1·82	1·78	2·03	23·0
Th	0·247	1·12	0·92	0·56	0·371	0·62	0·410	1·35	0·84	1·36	0·390	1·29
U	0·207	0·64	0·117	0·099	0·074	0·100	0·061	0·222	0·118	0·318	0·114	0·389

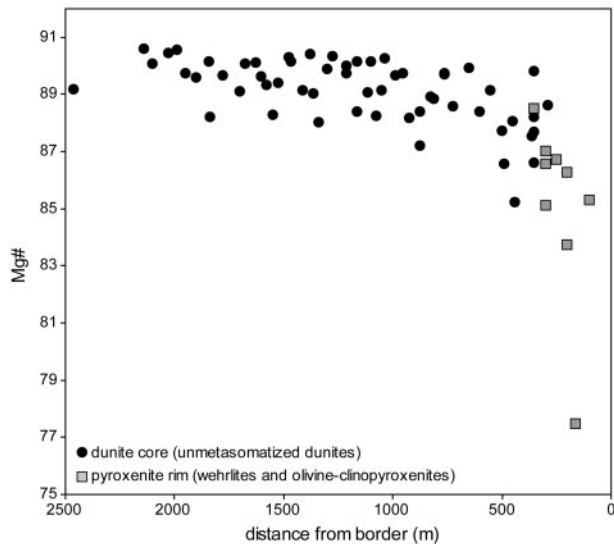LOI, loss on ignition, Mg-number = Mg/(Mg + Fe) cationic ratio; n.a., not analysed.

Fig. 8. Core-to-rim variation of Mg-number [Mg/(Mg + Fe) cationic ratio] in the Kondyor ultramafic body. Distances counted from the outer border of the pyroxenite rim; data from this study and from A. A. Efimov (unpublished data obtained by wet methods, Institute of Geology and Geochemistry, Ekaterinburg, Russia).
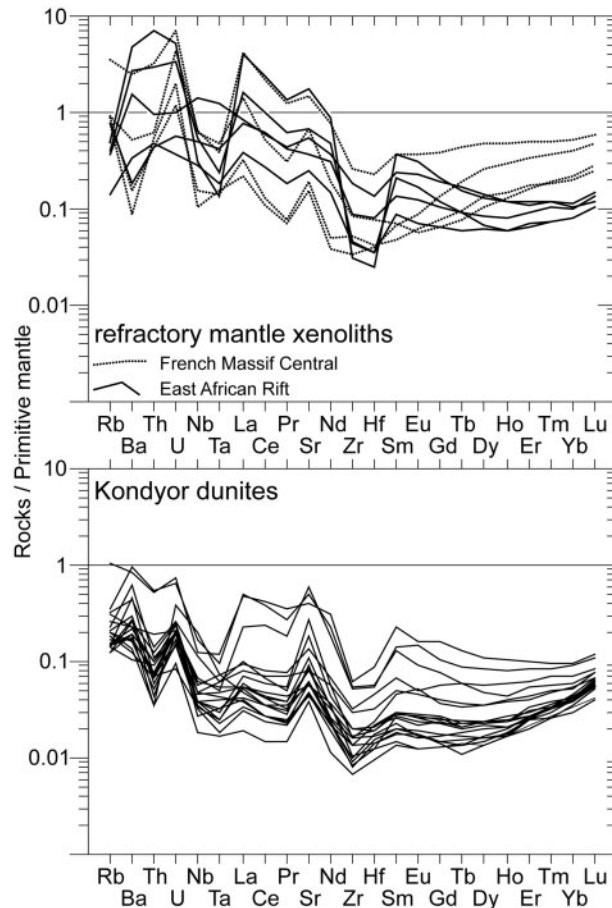

Fig. 9. Incompatible trace element contents of representative Kondyor dunites, normalized to primitive mantle values (Sun & McDonough, 1989). Comparison with other refractory mantle peridotite xenoliths from the Massif Central, France (Alard *et al.*, 1996) and the East African Rift (Bedini *et al.*, 1997).

wehrlites, all clinopyroxenites are enriched in Ca, Na, Al, Ti and incompatible trace elements (Table 3b; Fig. l0).

Overall, the rim wehrlites and clinopyroxenites are intermediate between the dunites and the intrusive clino-pyroxenites of the metasomatic domain in most of their incompatible-element contents, except for the highly incompatible elements Rb, Ba, Th and U that overlap the dunite composition (Fig. l0). Their PM-normalized trace-element signature, marked by deep HFSE negative anomalies, is comparable with the patterns of other rock types from Kondyor and the Aldan Shield lamproites (Davies *et al.*, 2006). In detail, however, the rim wehrlites and clinopyroxenites differ in having less enriched, or even depleted, contents of the most incompatible elements (Rb to LREE) relative to HREE. This is illustrated by the upward convexity of their REE patterns [LREE/MREE (middle REE) < PM ratio], whereas the dunites, for instance, display concave-upward patterns (LREE/MREE > PM ratio; Fig. 9). All rock types from the Kondyor rim differ from the dunites in having lower La/Yb values at a given La content (Fig. 1l). The offset from the dunite array is subtle for wehrlites but more significant for pyroxenites and related gabbros or syenites (see below) that define a positive correlation markedly distinct from that shown by the dunites.

Peripheral gabbros

Peripheral gabbros have higher Al, and lower Mg and Ca contents than the rim clinopyroxenites (Table 3). They are also strongly—although variably—enriched in the alkaline

and alkaline-earth elements Na, K, Rb, Cs, Sr and Ba. Their PM-normalized trace-element patterns resemble those of the rim clinopyroxenites but their concentrations are higher and the negative HFSE anomalies less marked (Fig. l0). As such, the peripheral gabbros resemble the gabbro dykes. Although less enriched in HIE (Rb to U), they also resemble the Aldan Shield lamproites. For most elements, the composition of the nephelinite syenite (sample K2l) lies on an extrapolation of the clinopyroxe-nite–gabbro trends towards low Mg-number and Ca values, and high Al, Na, K and incompatible trace-element contents. In addition, the syenite is virtually devoid of HFSE anomalies.

Metasomatic domain

Dunites from the metasomatic domain are compositionally comparable with the core dunites, but with a slightly wider range of Mg-number values (87·7–90·2). The lowest
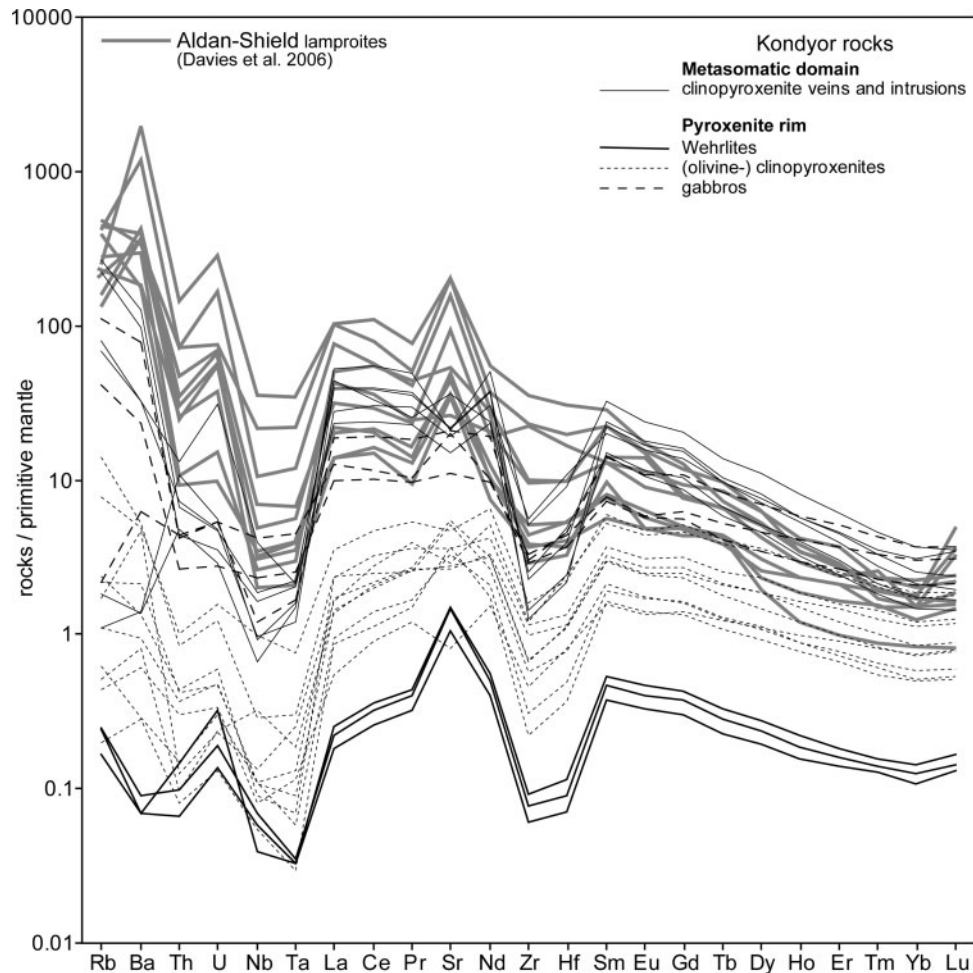
Fig. 10. Incompatible trace-element contents of Kondyor pyroxenites and representative igneous intrusions, normalized to primitive mantle values (Sun & McDonough, 1989), compared with lamproites from the Aldan Shield (Davies *et al.*, 2006).

Mg-number (87·7–88·7; Table 3) samples are rich in phlogopite (≥15%) and occur adjacent to clinopyroxenite veins (120p and 121d, from drill cores) or to the main bodies of intrusive clinopyroxenite (K29; Fig. 2). These samples are also distinguished by their low Ni contents (940–1200 ppm), comparable with the concentrations observed in the low-Mg-number, peripheral dunites. Metasomatized dunites tend to be more enriched in highly incompatible elements than the other dunites (Table 3). The strong enrichments in Rb, Cs and Ba in several samples are clearly related to the presence of phlogopite. However, most samples also tend to be enriched in LREE compared with other dunites (e.g. La and La/Yb in Fig. 11).

Clinopyroxenites from the metasomatic domain have low Mg-number (43·6–66), in the same range as the rim clinopyroxenites (Table 3). However, they are distinguished by variable trace element enrichments (Ti, Fe, K,

Rb, Cs, Sr, Ba and LREE) reflecting the relative abundance of phlogopite, Ti-oxides and apatite. Clinopyroxenites from the metasomatic domain also resemble the rim clinopyroxenites in terms of their trace-element signature, but their concentrations are much higher (Fig. 10). They are similar to the Aldan Shield lamproites with respect to REE, but display distinctive features for the other elements; that is, lower HIE abundances (Rb–Ta), more pronounced negative anomalies of Zr and Hf, and slightly negative anomalies of Sr, instead of positive anomalies.

Late dykes

Among the dykes that cut the dunites, the koswites and the hornblende gabbros are compositionally comparable with the clinopyroxenites of the metasomatic domain and the peripheral ring gabbros and syenites, respectively (Table 3). The koswites nevertheless differ from the
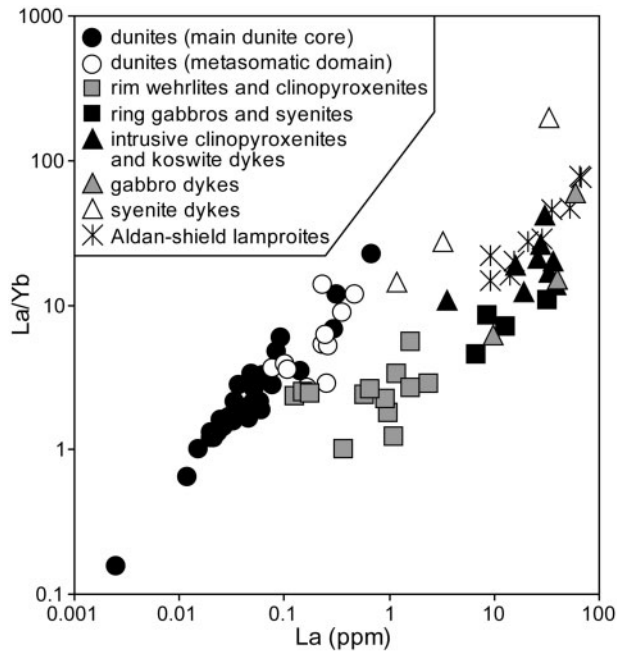
Fig. 11. La/Yb vs La diagram for Kondyor ultramafic rocks, related igneous intrusions and the Aldan Shield lamproites documented by Davies *et al.* (2006). This figure includes the authors' unpublished data on Kondyor gabbros and syenite dykes (analyses by ICP-MS at Géosciences Montpellier, AETE Regional Facility).

clinopyroxenites by slightly lower Mg-number (36·3–46·1; Table 2) whereas the gabbro dykes have even more variable Mg-number (15–70) than the rim gabbro–syenite suite. The syenite dykes differ from other rock-types in their more evolved major-element composition ($SiO_2 \sim 65\%$; MgO $\sim 1\%$; Mg-number ~ 20) and a strong depletion in HREE associated with slight positive anomalies of Zr, Hf and Ti, and a prominent Sr spike. The syenite dykes are further distinguished from clinopyroxenites and other igneous intrusions from Kondyor by their higher LREE/HREE values at a given REE content (Fig. 11). As such, they are paradoxically more akin to the ultramafic rocks, notably the wehrlites. Together with the clinopyroxenite bodies of the metasomatic domain, the other igneous dykes (koswites and hornblende-gabbros) overlap the composition of the Aldan-shield lamproites in Fig. 11. Although distinguished by higher La/Yb and La values, these rocks and the lamproites plot roughly on the same trend as that defined by the pyroxenites and gabbros or syenites of the rim.

DISCUSSION
Origin of dunites by olivine-forming melt–rock reaction
Based on its Mg-number, the central part of the dunite body was equilibrated with a primary mantle melt whereas the borders record a more evolved melt composition. However, the decreasing values of Mg-number and Ni content towards the margin (Fig. 8) are opposite to the variation commonly observed in zoned igneous intrusions, in which fractional crystallization proceeds from the colder, outer part towards the centre of the bodies. The Ni content of the dunites is notably lower than that of both cumulates from primary mantle melts and residual mantle rocks left after melt extraction. Both rock types are expected to show Ni contents in excess of 2000 ppm. In the cumulate hypothesis, the relatively low Ni content of the dunites would imply that their parental melt had previously undergone some degree of olivine fractional crystallization. However, Ni does not show the drastic drop observed in olivines of clear igneous origin at a given Mg-number (e.g. Kamenetsky *et al.*, 2008). Instead, the Ni content of the dunites (990–1620 ppm) shows a gentle, positive correlation with Mg-number (85·8–90·5). An important observation is that lower Mg-number values and Ni contents distinguish the phlogopite-bearing dunites adjacent to clinopyroxenite veins and intrusions in the metasomatic domain from their distal counterparts. This clearly indicates that the Mg-number–Ni covariation in dunites is governed by melt–rock interaction rather than by fractional crystallization. Numerical simulations of reactive porous flow (Godard *et al.*, 1995; Suhr, 1999) predict that olivine-forming, melt–rock reactions may account for low Ni contents in peridotites. Because of the partitioning of Ni in olivine preferentially to pyroxene, olivine precipitation combined with pyroxene dissolution results in Ni depletion hardly balanced by melt flow. Because of the compatible character of Ni and the chromatographic effects of melt transport, a high melt/rock ratio is indeed required to equilibrate a peridotite with incoming melt. Conversely, because it is partitioned into pyroxene preferentially to olivine, Cr may be substantially enriched during olivine-forming reactions (Godard *et al.*, 1995). The Mg-number is strongly buffered by olivine in peridotite–melt systems (Bodinier *et al.*, 2008) and may preserve the signature of the protolith even after high reaction degrees. Experimental studies (e.g. Stolper, 1980) have shown that liquids formed at depth by partial melting of four-phase peridotite become increasingly saturated in olivine ($\pm$ Cr-rich spinel) with decreasing pressure. Deep-seated partial melts migrating upward tend to dissolve the pyroxene component of percolated peridotites and crystallize olivine, leading to the formation of olivine-rich rocks (Kelemen, 1990). Olivine-forming reactions associated with magma transport are, therefore, considered to be the predominant dunite-forming mechanism (e.g. Kelemen, 1990).

In this scheme, the Kondyor dunites represent strongly reacted rocks from the sub-continental mantle. It is worth noting that, because of the strong dependence of

orthopyroxene stability on pressure (Kelemen, 1990), the reactivity of peridotite–melt systems is likely to be enhanced by translithospheric mantle upwelling, as long as primary pyroxene is not reacted out and the mantle body is not conductively cooled to subsolidus temperatures. In turn, the buoyancy of the upwelling body may be increased by partial melt produced along with olivine (Kelemen, 1990). This suggests that positive feedback relationships may exist between melt–rock reactions and upwelling of mantle rocks.

The Aldan Shield lamproites as reactant melt

Most ultramafic and igneous rocks at Kondyor, notably the clinopyroxenites from the metasomatic domain and the alkaline gabbros, show trace-element signatures comparable with those of lamproites (Fig. 10), suggesting a cogenetic relationship. The strong, MARID-type, K-metasomatism, characterized by abundant clinopyroxenite and glimmerite veins and phlogopite stockworks, also indicates that potassic melts have circulated in Kondyor. Waters (1987) suggested that high-pressure crystallization of ultrapotassic melts such as lamproites produced MARID xenoliths in kimberlites. Further information on the nature of the melts involved in the formation and evolution of the Kondyor suite may be retrieved from clinopyroxene compositions. These show two distinct differentiation trends: the first, characterized by high Al, Ca and Mg contents, includes clinopyroxenes from most of the pyroxenites and from the wehrlites, clinopyroxene-bearing dunites and glimmerite veins; the second, characterized by high Si, Fe and Na contents, is restricted to clinopyroxenes from apatite and/or carbonate-bearing clinopyroxenite veins. These two evolutionary trends diverge from a single, 'primary' diopside composition that coincides with the field of clinopyroxenes from lamproites (Bergman, 1987). These 'primary' clinopyroxene compositions are notably found in glimmerite veins and in the adjacent, metasomatized peridotites.

All these features converge on the idea that the mantle melt involved in the individualization of the Kondyor dunites and related rocks was akin to the 170–100 Ma Aldan Shield lamproites. This idea is consistent with the conclusions of Davies et al. (2006), who proposed that the origin of the lamproites was in the subcontinental lithospheric mantle. Some specific features of the lamproites might be related to the inferred reaction processes, such as the presence of olivine aggregates and their Mg-number ranging from 70 to 83.

Significance of the pyroxenite rim

Kelemen & Ghiorso (1986) and Jagoutz et al. (2006) have advocated reaction with melt infiltrated from outside the ultramafic bodies for the origin of the pyroxenites rimming ZUCs. Recent studies have documented the origin of certain types of mantle pyroxenite by pyroxene-forming reactions involving percolating melt (Garrido et al., 2007; Bodinier et al., 2008). Such reactions were probably involved in the formation of the Kondyor rim pyroxenites. First, the transition from dunite to differentiated clinopyroxenite cumulates is gradual, through clinopyroxene-bearing dunite and wehrlite with replacive textures (Fig. 4). Second, although showing strong similarities in their trace-element signature, all rim pyroxenites and wehrlites are distinguished from intrusive and vein pyroxenites by much lower abundance of incompatible trace elements (Fig. 10); the wehrlites also have much higher Cr abundances (615–2560 ppm, compared with 20–70 ppm; Table 3). As modelled by Garrido et al. (2007), the low incompatible trace-element contents may be accounted for by a reaction scheme involving two successive melt–rock reactions, resulting in the replacement sequence mantle peridotite $\rightarrow$ dunite $\rightarrow$ wehrlite–pyroxenite. In this scheme, wehrlites are generated via the peritectic reaction olivine + melt$_1$ $\rightarrow$ pyroxene + melt$_2$ with decreasing melt mass. This reaction is consistent with experimental work indicating that the parental melts of Cr-rich pyroxenites are saturated in olivine a few degrees above their crystallization temperature (Müntener et al., 2001). As pyroxene-forming, melt-consuming reactions can decrease the Mg-number of melt and peridotite in focused porous flow systems (Bodinier et al., 2008), wehrlite formation may also account for the relatively low-Mg-number aureole observed around the dunite body.

The existence of deformed cpx aggregates in the transitional, cpx-bearing dunites indicates that the Kondyor ZUC was pervasively percolated by melt and still deforming at high temperature when the pyroxenite rim was initiated. The localization of the cpx-forming, peritectic reaction at the border of the dunite body may be explained by the existence of a small conductive, thermal gradient around the massif. The initiation of the pyroxenite rim thus records early cooling at mantle depths, most probably within the lithospheric mantle. The differentiated clinopyroxenites with cumulate textures and the alkaline gabbros and syenites record polybaric crystallization of more evolved melts, residual after melt–rock reaction and further fractional crystallization. As a result of thermal contraction of the dunite body upon cooling, these melts were focused in the outer part of the massif, where they migrated up to shallow, crustal levels.

Late metasomatic and igneous processes

Only after substantial cooling of the Kondyor body were lamproite melts focused into vein conduits where they evolved by several mechanisms including wall-rock reaction, fractional crystallization and liquids unmixing. This last mechanism is inferred from the duality of the most

evolved mineralogical assemblages and cpx compositions in clinopyroxenite veins. This duality indicates that two contrasted liquids—nepheline-syenitic and carbonatitic—were generated upon differentiation of the primary lamproite melt. The simultaneous evolution of these two types of melts from volatile-rich alkaline magmas is commonly ascribed to the separation of immiscible liquids (e.g. Ferguson & Currie, 1970; Lee & Wyllie, 1997). The strong, selective HIE and LREE enrichment in the Kondyor dunites may be accounted for by entrapment of about 1% of such evolved melts, as indicated by the more enriched composition of dunites in the metasomatic domain, where clinopyroxenite and glimmerite veins are abundant (Fig. 11). This is further indication that the dunites were pervasively percolated by small melt volumes of syenitic or/and carbonatitic affinity during the late evolution of the Kondyor ZUC. These small melt fractions were mobile down to at least the relatively low lithospheric temperature at which the metasomatic domain was generated. Evolution of such HIE- and LREE-enriched small melt fractions from metasomatic domains and their pervasive percolation through the subcontinental lithospheric mantle has been proposed in a number of studies of mantle xenoliths and orogenic peridotites (e.g. Bedini *et al.*, 1997; Bodinier *et al.*, 2004).

Upon further cooling, thermal contraction of the ultramafic mass was associated with polybaric crystallization of variably evolved melts, including koswites, alkaline gabbros and nepheline syenites, both in ring intrusions and in cross-cutting dykes.

Significance of structures and textures

The petro-structural study indicates that the Kondyor dunites were deformed by solid-state flow under deep-lithospheric to asthenospheric conditions. The outward textural change from coarse- to fine-grained, equigranular dunite and the outward-increasing abundance of subgrains and recrystallized olivine grains suggest that dynamic recrystallization induced grain-size reduction (Harte, 1977). This textural distribution additionally suggests that fluid circulation was channelized within the core and in the metasomatic zone, whereas solid-state deformation was concentrated at the border of Kondyor ZUC during its late-stage evolution. As such, the petro-structural data support the interpretation of a high-temperature mantle intrusion triggered by fluid pressure channelized in the core and associated hydrofracturing. The flat foliation suggests that the present level of erosion exposes the domal top of the intrusion, and that the synformal structure could result from internal sagging. Concentric lineations could indicate vortex flow (e.g. Hippertt, 1994) either during ascent or during sagging of the ultrabasic rocks.

INTERPRETATION—STATEMENT OF THE MECHANICAL PROBLEM

The Kondyor ZUC has been explained by crystal fractionation of a picritic melt in a magma chamber (e.g. Orlova, 1992). However, the textural and petro-structural characteristics of the ultramafic rocks indicate that the Kondyor dunite was emplaced at the final stage as a solid mass, such that magma pressure cannot be invoked to explain doming of the regional sedimentary basement. In addition, the absence of dunite or pyroxenite dikes in the country rocks argues against simple magmatic intrusion, even if the contact metamorphic aureole indicates that the Kondyor ZUC intruded the upper crust up to *c.* 2 km depth as a hot body.

Structural, petrographic and geochemical information converge on the idea that the Kondyor ZUC has been forcefully emplaced through the continental crust. We envisaged the following scenario. The dunite core was first individualized in a porous melt reservoir at the base of the lithospheric mantle, possibly eroded by a mantle plume. The lithospheric mantle rocks reacted strongly with melts of deep-seated origin. Instabilities triggered by the accumulation of volatile-rich melt forced the dunite into the crust as a translithospheric diapir. The rim pyroxenites were formed via a peridotite, cpx-forming reaction involving melts pervasively circulating through the dunites. This reaction indicates conductive cooling of the dunite rim upon upwelling of the Kondyor ZUC into the lithosphere. The central metasomatic domain is considered as a dying feeder channel for relatively primitive melts focused in the ZUC medial spine. The mechanism that generated a vertical column of dense ultramafic rocks within the lithosphere nearly to the surface remains, however, enigmatic. Numerical modelling was therefore carried out to explore the mechanical and thermal conditions under which translithospheric diapirism is plausible.

NUMERICAL MODELLING

We employed the 2D code I2ELVIS (Gerya & Yuen, 2003) specifically adapted to simulate the intrusion of partially molten mantle rocks from a sub-lithospheric magmatic source region (SMSR, Fig. 12, 0 kyr; Gerya & Burg, 2007). The modeled SMSR is a thermally and chemically distinct region of hydrated, partially molten mantle rocks, not a chamber of fully molten magma. Partially molten mantle material has a much lower viscosity than the surrounding solid mantle (e.g. Pinkerton & Stevenson, 1992) and can move upward through a channel as a crystal mush. In this sense the SMSR is equivalent to a magma reservoir. According to the linear melting model we employ (Gerya & Burg, 2007) this partially molten region has 10–30 vol.% melt, depending on depth and temperature. Although the bulk composition of the SMSR is ultramafic, the melt
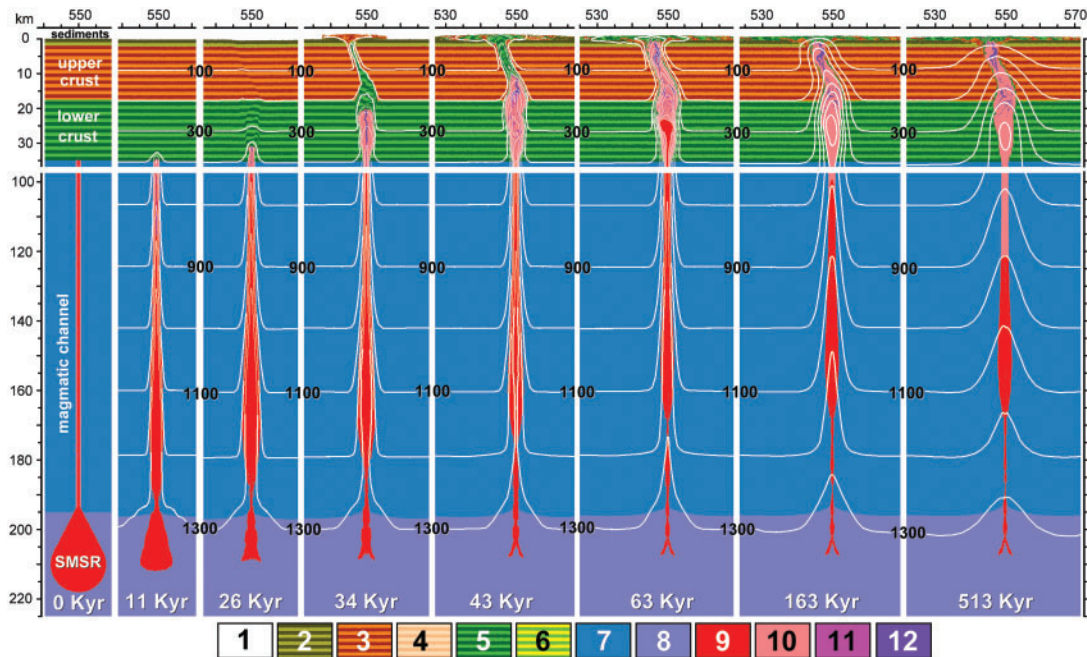
Fig. 12. Enlarged (20–50) km × 225 km areas of the original 1100 km × 300 km reference Model 11 (Table 5). Distribution of rock layers in the intrusion area during emplacement of the ultramafic body into the crust from below the lithosphere via the magmatic channel. Colour code: 1, weak layer (air, water); 2, sediments; 3, 4, upper crust (3, solid; 4, molten); 5, 6, lower crust (5, solid; 6, molten); 7, 8, mantle (7, lithospheric; 8, asthenospheric); 9, 10, peridotite (9, molten; 10, crystallized); 11, 12, gabbro (11, molten; 12, crystallized). Time (kyr) is given in the figures. White numbered lines are isotherms (in °C). Vertical scale: depth below the upper boundary of the model (in km).

composition depends on the degree of melting and thus varies between mafic and ultramafic. The general code is based on finite-differences with a marker-in-cell technique and allows for the accurate conservative solution of the governing equations on a rectangular fully staggered Eulerian grid. Developments introduced for intrusion simulation allow for both large viscosity contrasts and strong deformation within a visco-elasto-plastic multiphase flow, incorporating temperature-dependent rheologies of both intrusive molten rocks and host-rocks (Gerya & Burg, 2007). The magmatic channel is modelled as a vertical, 1·5 km wide zone characterized by a wet olivine rheology and a low 1 MPa plastic strength throughout the lithospheric mantle. The initial thermal structure of the lithosphere is as usually assumed, with a 35 km thick crust (Fig. 12, 0 kyr) corresponding to a sectioned linear temperature profile limited by 0°C at the surface, 400°C at the bottom of the crust and 1300°C at 195 km depth. The temperature gradient in the asthenospheric mantle is 0·6°C/km below 195 km depth. Material properties are given in Table 4.

In addition to the 40 models previously performed to constrain intrusion of ultramafic bodies into the crust (Gerya & Burg, 2007), 46 additional numerical experiments have been run with a finite-difference grid of 325 × 125 irregularly spaced Eulerian points, and with 3·5 million markers to portray fine details of the temperature,

material and viscosity fields (for the parameters of the 12 cases discussed in this study, see Table 5).

The code colour identifying specific rock types is given in Fig. 12. The discrimination between 'molten peridotite' and 'peridotite' is thermal, separating material points (pixels) above and below the wet solidus temperature of peridotite (Table 4) at a given pressure, respectively. Because the melt fraction changes strongly with the water content, variations within a few per cent of the melt fraction at any given pressure–temperature conditions have to be envisaged. Therefore, it is illusory to predict the exact melt fraction at any point of the models, in particular because the simplified linear melting model implemented here does not allow a very high precision on this question (Gerya & Burg, 2007).

Application to the Kondyor ZUC

Selecting Model kofz (Model 11 in Table 5, Figs 12 and 13) as that which best fits the Kondyor ZUC was, as a first approach, based on identification of the models whose final stages correctly replicate the available geological and geophysical information; that is, the existence of a <10 km diameter column of ultramafic rocks up to 2–3 km depth in the crust (Fig. 13). Other constraints were the preservation of basement slivers around the peridotite body, a narrow thermal aureole around it and slightly asymmetrical, concentric zoning with a fluid-rich medial zone.

Table 4: Material properties used in 2D numerical models

Material	ρ_0 (kg/m^3)	K [W/(m K)]	$T_{solidus}$ (K)	$T_{liquidus}$ (K)	Q_L (kJ/kg)	H_r (μW/m^3)	Flow law	E (kJ/mol)	n	A_D (MPa^{-n}/s)	V [J/(MPa mol)]	μ (GPa)
Sediments	2600	$[0.64+807/(T+77)]$ $\times \exp(0.00004P_{MPa})$	—	—	—	1.75	wet quartzite	154	2.3	$10^{-3.5}$	0	10
Felsic crust	2800 (solid)	$[0.64+807/(T+77)]$ $\times \exp(0.00004P_{MPa})$	$889+17900/(P+54)$ $+20200/(P+54)^2$ at $P<1200$ MPa,	$1262+0.09P$	300	1	wet quartzite	154	2.3	$10^{-3.5}$	0	25
	2500 (molten)		$831+0.06P$ at $P>1200$ MPa									
Mafic crust, gabbro of the magma chamber	3000 (solid)	$[1.18+474/(T_K+77)]$ $\times \exp(0.00004P_{MPa})$	$973-70400/(P+354)$ $+77800000/(P+354)^2$ at $P<1600$ MPa,	$1423+0.105P$	380	0.25	plagioclase An$_{75}$	238	3.2	$10^{-3.5}$	0	25
	2800 (molten)		$935+0.0035P+$ $0.0000062P^2$ at $P>1600$ MPa									
Lithosphere–asthenosphere mantle	3300	$[0.73+1293/(T_K+77)]$ $\times \exp(0.00004P_{MPa})$	—	—	—	0.022	dry olivine	532	3.5	$10^{4.4}$	8	67
Peridotite of the magma chamber	3250 (solid)	$[0.73+1293/(T_K+77)]$ $\times \exp(0.00004P_{MPa})$	$1240+49800/(P+323)$ at $P<2400$ MPa,	$2073+0.114P$	300	0.022	wet olivine	470	4	$10^{3.3}$	8	67
	2900 (molten)		$1266-0.0118P$ $+0.0000035P^2$ at $P>2400$ MPa									
References*	1, 2	3	4	4, 6	1, 2	1	5	5	5	5	1, 5	1

C_p = 1000 J/kg, $\alpha = 3 \times 10^{-5}$ K^{-1}, $\beta = 1 \times 10^{-5}$ Mp/a for all rock types. Definitions of parameters have been given by Gerya & Burg (2007).
*1, Turcotte & Schubert (2002); 2, Bittner & Schmeling (1995); 3, Clauser & Huenges (1995); 4, Schmidt & Poli (1998); 5, Ranalli (1995); 6, Hess (1989).

Table 5: Parameters of selected numerical experiments

Model	Upper crust	Lower crust	SMSR				Upper crust			Lower crust			T Moho	Shape*	Magmatic body	
			Diameter (km)	C (MPa)	h_{min} (Pa s)	T_0 (°C)	λ_0	C (MPa)	γ_{cr}	λ_0	C (MPa)	γ_{cr}	(°C)		Depth (km)	Diameter (km)
1 (kofh)	felsic	mafic	16	0·5	10^{13}	1400	0·33	1	0·1	0·67	0·5	0·1	400	I	0	3·1–5·8
2 (kofi)	felsic	mafic	17	0·5	10^{13}	1400	0·33	1	0·1	0·67	0·5	0·1	400	I	0	3·7–6·6
3 (kofj)	felsic	mafic	18	0·5	10^{13}	1400	0·33	1	0·1	0·67	0·5	0·1	400	I–T	0	4·0–14·0
4 (kofk)	felsic†	mafic	16	0·5	10^{13}	1400	0·33	1	0·1	0·67	0·5	0·1	400	I-S	4·6	3·4–6·4
5 (kofl)	felsic	mafic	16	0·5	10^{13}	1400	0·50	1	0·1	0·67	0·5	0·1	400	V	4·8	4·2–12·3
6 (kofm)	felsic	mafic	16	0·5	10^{13}	1400	0	1	0·1	0·67	0·5	0·1	400	I–V	2·4	3·5–9·5
7 (kofn)	felsic	mafic	15	0·5	10^{13}	1350	0·33	1	0·1	0·67	0·5	0·1	400	I	5·9	3·6–6·6
8 (kofo)	felsic	felsic	16	0·5	10^{13}	1400	0·17	1	0·1	0·67	0·5	0·1	400	I	0	3·3–5·1
9 (kofp)	felsic	mafic	18	0·5	10^{13}	1400	0	1	0·1	0·67	0·5	0·1	400	V	0·5	3·4–13·9
10 (kofx)	mafic	mafic	16	0·5	10^{13}	1400	0·33	100‡	0·1	0·67	0·5	0·1	400	I–T	0	3·6–9·9
11 (kofz)	felsic	mafic	16	0·5	10^{13}	1400	0·33	100‡	0·1	0·67	0·5	0·1	400	I	1	2·9–6·5
12 (kogf)	mafic	mafic	18	0·5	10^{13}	1400	0	100‡	0·05	0·67	0·5	0·05	400	T	17·4	4·5–55

*Final shape of the body after emplacement (Fig. 14): V, funnel-shaped; S, sickle-shaped; I, finger-shaped; T, sill-shaped.
†Lowered thickness of the upper crust (8 km).
‡Decreases linearly to 0·5 MPa with plastic strain increasing from zero to γ_{cr}.
Definitions of parameters have been given by Gerya & Burg (2007).
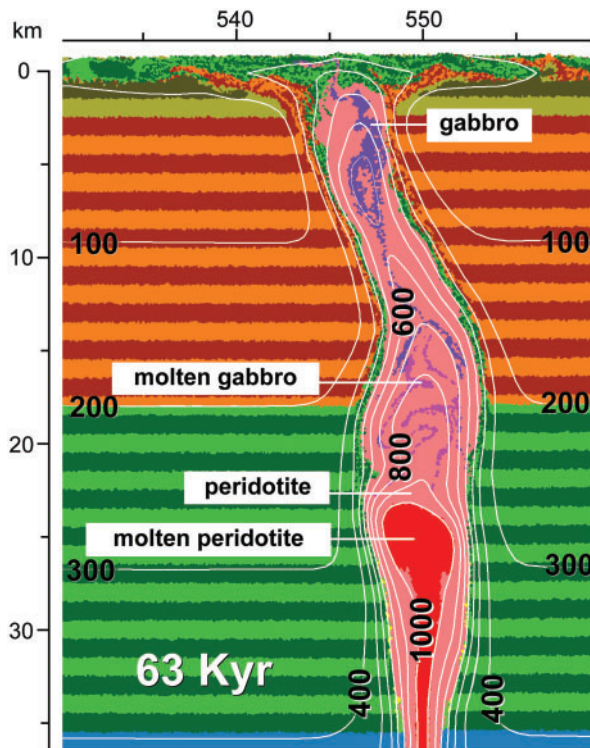
Fig. 13. Temperature distribution around intrusion during the emplacement stage at 63 kyr. Enlarged 28 km × 35 km area of the original 1100 km × 300 km reference Model 11 is shown (Fig. 12; Table 5). White numbered lines are isotherms (in °C). Colour code is the same as in Fig. 12.

Further constraints were based on the fact that the partially molten rocks that produced the Kondyor peridotites have intruded the lower crust, possibly up to the middle crust, but not the upper crust. A structural argument in this sense is that ultrabasic rocks able to intrude the upper crust would probably be intrusive 'mushes' with olivine phenocrysts, in contrast to the strongly reacted mantle rocks found in Kondyor. Model kofz fulfils all these requirements.

Like previous simulations of mafic–ultramafic intrusions involving a wide range of parameters (Gerya & Burg, 2007), model kofz consists of three successive stages (Fig. 12): (1) magmatic channel spreading (Fig. 12, 0–26 kyr); (2) crustal emplacement (Fig. 12, 26–63 kyr); (3) post-intrusive subsidence (Fig. 12, 63–513 kyr). Channel spreading is a rapid event (10–20 kyr). The density contrast between partially molten rocks in the sub-lithospheric magma source region and the surrounding mantle lithosphere drives the upward expulsion of hot, high-density rocks up to the crust–mantle boundary. Crustal emplacement begins when the rising mantle rocks impinge on the lower crust (Fig. 12, 26 kyr). This creates upward propagating, vertical, subparallel faults and shear zones between which mantle rocks and magma penetrate the lower crust while pushing up a spine of lower-crustal rocks into the brittle upper crust (Fig. 12, 26–43 kyr). Upward-diverging conjugate faults form at shallow depth and cause the slightly curved, widening-up shape of the intrusion top.
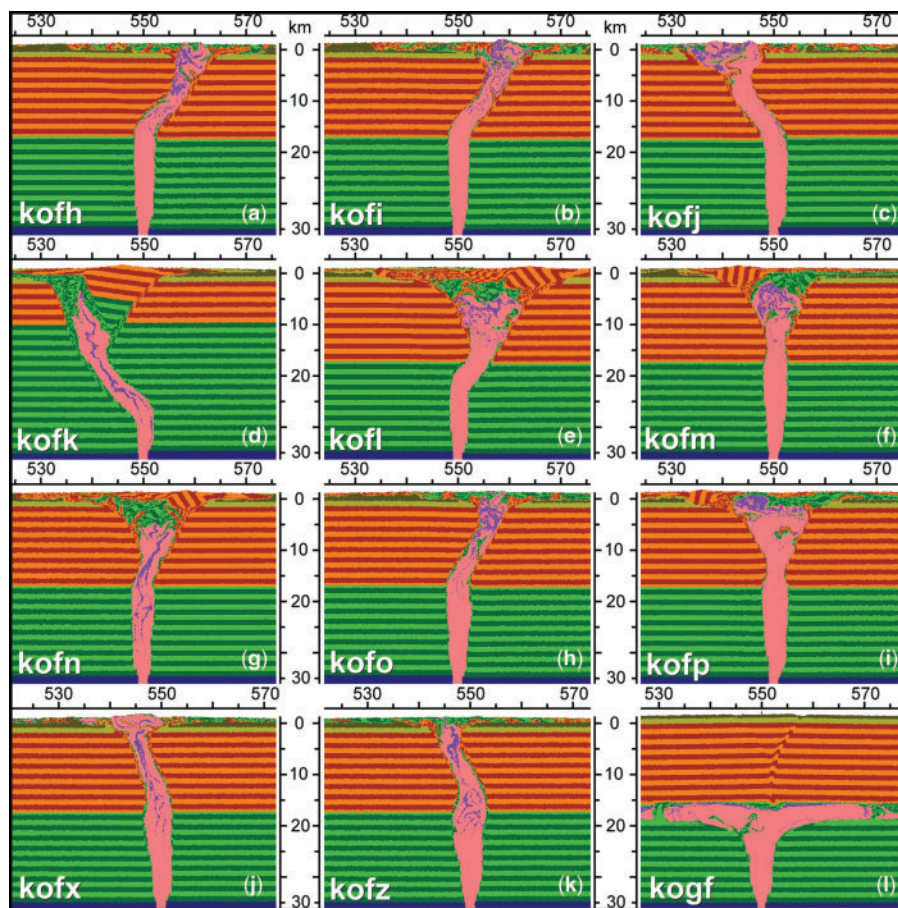
Fig. 14. Variations in final shapes and internal geometry of intrusions with varying numerical model parameters (Table 5). Colour code is the same as in Fig. 12.

Ultramafic and mafic rocks follow the extruded and eroded lower crustal spine and intrude the upper crust up to near-surface conditions within *c.* 63 kyr (Fig. 12). Intrusion ceases and is followed by minor thermal subsidence.

In all models, the angle and the depth of the fault divergence strongly depend on the brittle strength of the upper crust, and hence on the initial pore fluid pressure (Gerya & Burg, 2007): the weaker the upper crust, the deeper the divergence point. In other words, funnel-shaped, deep intrusions (e.g. Model 5, kofl, Table 5, Fig. 14e) rather than finger-shaped shallow bodies (Model 11, kofz, Table 5, Fig. 14k) characterize a weak upper crust. In a strong upper crust, one of the conjugate faults tends to dominate the system, propagating toward the surface while deformation along the other conjugate fault vanishes. An unambiguous result of all the experiments is that the emplacement of columnar, finger-like intrusions is ruled by the elasto-plastic behaviour of the intruded crust at every level. In such a case, subvertical emplacement

minimizes the mechanical work during intrusion. This is confirmed by varying the initial cohesion of the upper crust (compare models kofh and kofz; Models 1 and 11 in Table 5; Fig. 14a and k); the body tends to be vertical with larger cohesion. Further increase in the plastic strength of the upper crust may actually block vertical propagation of the body, which then forms sill-shaped intrusions at the boundary between the upper and lower crust (kogf, Model 12 in Table 5, Fig. 14).

Vertical propagation of high-density ultramafic intrusions in lower density continental crust, in the absence of far-field tectonic forces, is explained by the distribution of non-lithostatic pressure around the partially molten SMSR and the magmatic channel (Fig. 15), which are both characterized by densities lower than that of the mantle lithosphere. Two important features characterize the pressure distribution: (1) a relative underpressure in the incompressible SMSR, which is therefore pushed up through the channel by the host mantle replacing the SMSR; (2) strong overpressure at the top of the channel, which drives
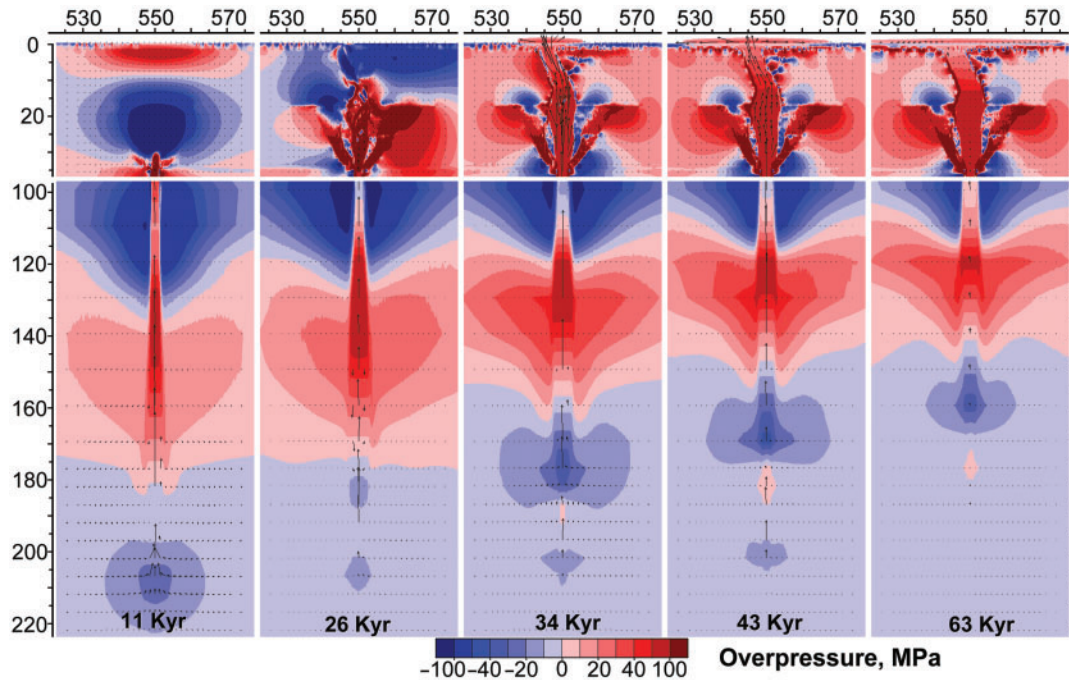
Fig. 15. Distribution of non-lithostatic pressure component around the intrusion and the SMSR for emplacement stages from 11 to 63 kyr. Enlarged 57 km × 225 km areas of the original 1100 km × 300 km reference Model 11 are shown (Fig. 12, Table 4).

magma penetration into the comparatively lower pressured crust. The strong positive buoyancy of the SMSR with respect to the overlying mantle lithosphere governs this pressure distribution. This is markedly different from the case where production of fluid-rich melts in the SMSR builds up high fluid pressure, which precludes substitution by the surrounding mantle and enhancement of escape of the molten fraction into the (forming) magmatic channel (e.g. Wilson & Head, 2007). In the models presented here, strong pressure gradients in the crust favour propagation of melts outward from the magmatic channel so that the emplacement work is minimized: it is upward in an elasto-plastic crust (Fig. 15) and sideways in a low-viscosity crust (Gerya & Burg, 2007).

Acceptable shortcomings of model kofz concern the attitude of the body (subvertical in Kondyor and inclined in the model), the internal rock distribution, the synformal final shape and the rim plutons. The vertical attitude is prominent in less preferred models kofm and kofn (Models 6 and 7 in Table 5; Fig. 14f and g). These models had, however, important caveats concerning the depth that molten rocks reach, the shape (rather than a funnel) and depth of emplacement. For example, a huge block of lower crustal rocks caps the ultrabasic rocks of kofn, which is inconsistent with the geological information. The vertical attitude in the crust actually depends on both the brittle strength of the crust and on the size of the SMSR: the stronger the crust (compare Model 1, kofg and Model 6, kofl, Table 5; Fig. 14a and e) and/or the larger the SMSR (compare Models 1, kofh and 7, kofn, Table 5; Fig. 14a and g; Models 6, kofm and 9, kofp, Table 5; Fig. 14f and i) the higher the vertical intrusion can rise.

The lithological and structural zoning of the Kondyor massif is more asymmetric than in model kofz. Asymmetrical zoning is a result of models kofm and kofp (Models 6 and 9 Table 5; Fig. 14f and i) whose final states, however, do not replicate the general, near-surface structure of Kondyor and for which the molten rocks would rise too high. Model kofz reproduces the prevalence of ultramafic rocks surrounded by basic rocks and deep crustal wedges dragged up along the intrusion boundaries to the surface. Basic (gabbro) igneous rocks are concentrated in a medullar channel, at the core of the column, in a position equivalent to the koswite-rich metasomatic zone of Kondyor. Indeed, a model 'gabbro' means lower density, more fluid-rich magma, which compositionally fits this metasomatic zone and is probably the source for the platinoids. Other mafic rocks occur at the edges of the ultramafic rocks, simulating the peripheral, reactive pyroxenites and the general concentric zoning of the Kondyor ZUC. The external ring of pyroxenites seals the ductile deformation of the dunites and attests to early, and thus deep circulation of fluids along the walls of the 'diapir'.

These fluids probably assist the rise of the ultramafic body, a lubricating effect that was not implemented in our model.

The olivine fabric reflecting concentric down-flow in the dunite whose foliation pattern describes a large synform inconsistent with the domal structure of Kondyor represents solid-state return down-flow during post-intrusion flattening and subsidence, which is quickly suppressed by the increasing strength of the crystallizing magma. The final synformal shape obtained in kofi, kofj and kofl (Models 2, 3 and 5, Table 5; Fig. 14b, c and e) is less pronounced in kofz, which reflects incompressibility and, subsequently, less subsiding and spreading of magma at the final shallowest emplacement level.

The limited amount of crustal melting involved in the most appropriate models actually suits the small size of the felsic intrusions around Kondyor (compare lower crustal melting around the intrusion in Fig. 13). These small intrusions are either derived from later crustal melting or are the most mobile magmas from the magma source region that have taken advantage of fracture zones forming in front of the rising ultramafic body, while space was created by thinning and separation of fault blocks in the crust (Fig. 12, 16–22 kyr). Discriminating geochronological information is lacking.

Another point for discussion concerns the head of the model 'diapir' that generates important deformation of the near-surface crust over a wide area. The 2D models overemphasize the size of the deformed area, compared with what it would be in three dimensions. In three dimensions, the faults controlling emplacement will tend to be concentric. We have planned additional 3D models to improve our understanding of magmatic channels and emplacement processes, preserving, however, the essential features quantified in this study.

Consequences of the model kofz

Model kofz is numerically characterized by a strong upper crust with a low pore fluid pressure factor, more than two times lower than that in the lower crust. The SMSR has a moderate size (16 km diameter; Table 5). Changes in these two parameters significantly affect both the final model geometry and the emplacement depth (Table 4, Fig. 14). The ductile flow law of the crust (Table 5) plays a subordinate role. These numerical conditions limit the parameter space for Kondyor-like models. The lower and especially the upper continental crust should be sufficiently dry and cold to have a high initial plastic strength and to focus strongly intrusion between subvertical faults. Consequently, surface deformation is also localized, as the faults do not propagate laterally from the emplacement area. These requirements for a naturally very strong crust are consistent with the Precambrian craton that has hosted Kondyor.

The distinctive feature of Kondyor is its nearly perfect circular (columnar) shape, which may additionally reflect the absence of far-field stresses in the crust. Such conditions are expected for anorogenic (A-type) magmatism, which is particularly common in Proterozoic terranes (e.g. Eby, 1990). The assumed magmatic channel at the beginning of the process may represent any rheological discontinuity (tectonic or lithological) arguably existing in an old continental craton such as the Aldan Shield.

The other distinct and economically valuable feature of Kondyor is the high concentration of platinum-group elements (PGE) in the eroded tip, and lower concentrations in the remaining metasomatic zone. This study indicates that uprise of the Kondyor massif was intrinsically associated with solid–melt reactions involving subcontinental peridotites and lamproitic partial melts as initial reactants. These reactions generated a series of variably evolved melts, which drained into vein and dyke systems during the late evolutionary stages of the massif. Interestingly, the millimetre-sized crystals of Pt–Fe alloy found in Kondyor contain as inclusions the same secondary phases (fluorapatite, titanite, phlogopite, magnetite, ilmenite and iron–copper sulphides; Shcheka *et al.*, 2004) as the intrusive igneous rocks, notably the apatite–oxide clinopyroxenites and koswites. In agreement with the preferential concentration of Pt–Fe alloys in the LREE-enriched metasomatic domain (Nekrasov *et al.*, 1994), this feature indicates that the Kondyor PGE ores were precipitated from the LREE-enriched, volatile-rich differentiates formed via crystal segregation in veins and wall-rock reaction in the cooling, upper part of the intrusion.

The intrusion model developed for Kondyor is potentially applicable to other types of magmatic rock that originated at sub-lithospheric depths. Olivine xenocrysts in kimberlites, for example, have been attributed to olivine crystallization and melt–rock interaction (Arndt *et al.*, 2006). Such interaction is apparent in the high-resolution numerical model of Fig. 13, where fragments of various mantle and crustal rocks are present along the margins and in the interior of the crystallizing, partially molten ultramafic body. In that respect, the Kondyor body may help to understand what happens in kimberlites during their ascent from deep in the mantle, before they reach the crustal levels where volume changes as a result of magma degassing under lowering pressure start playing a major role in intrusion geometry and eruption dynamics (Wilson & Head, 2007). At variance with the kimberlite model, fracturing of the country rocks in our model is caused by magma overpressure (Fig. 15) resulting from the inherent pressure distribution in the vertical low-density magmatic channel penetrating high-density lithospheric rocks. Fracturing decreases the brittle strength of the crustal rocks and aids further upward

penetration of the intrusion (pipe, dyke) towards shallower levels (Fig. 12).

CONCLUSION

The results of this study show that translithospheric diapirism, as envisioned for the Kondyor ZUC, is a viable emplacement mechanism that does not require a major tectonic event and may account for the genesis of other zoned ultramafic complexes, in particular the Alaskan-type ZUCs with which Kondyor shares many structural and petrological features. Neither significant lithospheric thinning nor a long incubation time of a mantle plume at the base of the lithosphere is essential to trigger translithospheric diapirism. In fact, the envisioned process may strongly depend on the existence of ancient lithospheric relief at the asthenosphere–lithosphere boundary, which would provide an explanation for the close relationship between the spatial distribution of zoned ultramafic complexes and older major tectonic trends (Butakova, 1974; Elianov & Andreev, 1991).

Our preferred model provides an explanation for the strong positive gravity anomalies associated with a number of 'ring-shaped' complexes occurring at continental margins (e.g. Geoffroy, 1998). In this scheme, translithospheric mantle diapirism should be a common mechanism for the initiation of continental rifting (e.g. Lallemant, 1985) and subsequent lithospheric break-up above mantle plumes. In subduction-related environments, it could be responsible for magmatic arc splitting (e.g. Burg *et al.*, 1998). Although our calculations were tuned for finger-like structures, we expect that sheet-like translithospheric diapirs may form where large fissures occur, such as the several hundred kilometres long Jurassic dykes formed during opening of the Atlantic Ocean in Iberia (e.g. Schermerhorn *et al.*, 1978; Cebria *et al.*, 2003) and Morocco (e.g. Aarab *et al.*, 1994; Silva *et al.*, 2004). Translithospheric diapirism may also explain the structures identified on Venus (e.g. Phillips & Hansen, 1998; Ernst & Desnoyers, 2004, 2009) and large volcanoes such as Olympus Mons on Mars reported to be, along with other Mars volcanoes, underlain by anomalously dense lithosphere (Blasius & Cutts, 1981).

Other implications may concern melt extraction from the mantle, with new constraints on the focusing mechanism of vertical melt flow. This may be even more significant for the mobilization and concentration of PGE, with implications on the processes whereby these elements, of high economic value, are drained from the mantle and segregated into zoned complexes.

ACKNOWLEDGEMENTS

REFERENCES

Aarab, E. M., Rahimi, A. & Rocci, G. (1994). Un exemple de différenciation transverse: le Grand Dyke de Foum Zguid (Anti-Atlas, Maroc). *Comptes Rendus de l'Académie des Sciences, Série II* **319**, 209–215.

Alard, O., Dautria, J.-M. & Bodinier, J.-L. (1996). Nature of the upper mantle and metasomatic processes on either side of the Sillon Houiller (French Massif Central). *Comptes Rendus de l'Académie des Sciences* **323**, 763–770.

Arndt, N., Boullier, A.-M., Clément, J. P., Dubois, M. & Schissel, D. (2006). What olivine, the neglected mineral, tells us about kimberlite petrogenesis. *eEarth* **1**, 15–21.

Batanova, V. G., Pertsev, A. N., Kamenetsky, V. S. A., Ariskin, A., Mochalov, A. G. & Sobolev, A. V. (2005). Crustal evolution of island-arc ultramafic magma: Galmoenan pyroxenite–dunite plutonic complex, Koryak Highland (Far East Russia). *Journal of Petrology* **46**, 1345–1366, doi:1310.1093/petrology/egi1018.

Bedini, R. M., Bodinier, J.-L., Dautria, J.-M. & Morten, L. (1997). Evolution of LILE-enriched small melt fractions in the lithospheric mantle: A case study from the East African Rift. *Earth and Planetary Science Letters* **153**, 67–83.

Bergman, S. C. (1987). Lamproites and other potassium-rich igneous rocks: a review of their occurrence, mineralogy and geochemistry. In: Fitton, G. J. & Upton, B. G. J. (eds) *Alkaline Igneous Rocks. Geological Society, London, Special Publications* **30**, 103–190.

Bhattacharji, S. & Smith, C. H. (1964). Flowage differentiation. *Science* **145**, 150–153.

Bittner, D. & Schmeling, H. (1995). Numerical modeling of melting processes and induced diapirism in the lower crust. *Geophysical Journal International* **123**, 59–70.

Blasius, K. R. & Cutts, J. A. (1981). Topography of Martian central volcanoes. *Icarus* **45**, 87–112.

Bodinier, J.-L., Menzies, M. A., Shimizu, N., Frey, F. A. & McPherson, E. (2004). Silicate, hydrous and carbonate metasomatism at Lherz, France: Contemporaneous derivatives of silicate melt–harzburgite reaction. *Journal of Petrology* **45**, 299–320.

Bodinier, J.-L., Garrido, C. J., Chanefo, I., Bruguier, O. & Gervilla, F. (2008). Origin of pyroxenite–peridotite veined mantle by refertilization reactions: evidence from the Ronda peridotite (Southern Spain). *Journal of Petrology* **49**, 999–1025.

Boullier, A. M. & Nicolas, A. (1973). Textures and fabrics of peridotite nodules from kimberlite at Mothae, Thaba Putsoa and Kimberley. In: Nixon, P. H. (ed.) *Lesotho Kimberlites*. Maseru: Lesotho National Development Corporation, pp. 57–66.

Burg, J.-P., Bodinier, J.-L., Chaudhry, M. N., Hussain, S. & Dawood, H. (1998). Infra-arc mantle–crust transition and intra-arc mantle diapirs in the Kohistan Complex (Pakistani Himalaya): petro-structural evidence. *Terra Nova* **10**, 74–80.

Butakova, E. L. (1974). Regional distribution and tectonic relations of the alkaline rocks of Siberia. In: Sørensen, H. (ed.) *The Alkaline Rocks*. New York: John Wiley, pp. 172–189.

Cabri, L. J. & Laflamme, J. H. G. (1997). Platinum-group minerals from the Konder Massif, Russian Far East. *Mineralogical Record* **28**, 97–106.

Cebria, J. M., Lopez-Ruiz, J., Doblas, M., Martins, L. T. & Munha, J. (2003). Geochemistry of the Early Jurassic Messejana–Plasencia dyke (Portugal–Spain); Implications on the origin of the

Central Atlantic Magmatic Province. *Journal of Petrology* **44**, 547–568.

Clauser, C. & Huenges, E. (1995). Thermal conductivity of rocks, minerals. In: Ahrens, T. J. (ed.) *Rock Physics and Phase Relations*, American Geophysical Union, Washington, DC, pp. 105–126.

Davies, G. R., Stolz, A. J., Mahotkin, I. L., Nowell, G. M. & Pearson, D. G. (2006). Trace element and Sr–Pb–Nd–Hf isotope evidence for ancient, fluid-dominated enrichment of the source of Aldan shield lamproites. *Journal of Petrology* **47**, 1119–1146.

Dawson, J. B. (1987). The MARID suite of xenoliths in kimberlite: relationship to veined and metasomatised peridotite xenoliths. In: Nixon, P. H. (ed.) *Mantle Xenoliths*. Chichester: John Wiley, pp. 465–473.

Dawson, J. B. & Smith, J. V. (1977). The MARID (mica–amphibole–rutile–ilmenite–diopside) suite of xenoliths in kimberlite. *Geochimica et Cosmochimica Acta* **41**, 309–323.

Eby, G. N. (1990). The A-type granitoids: A review of their occurrence and chemical characteristics and speculations on their petrogenesis. *Lithos* **26**, 115–134.

Efimov, A. A. & Tavrin, I. F. (1978). On genetic unity of platinum-bearing dunites of the Urals and Aldan Shield. *Doklady Akademii Nauk SSSR* **243**, 991–994, (in Russian).

Efimov, A. A., Efimova, L. P. & Mayegov, V. I. (1993). The tectonics of the Platinum-Bearing Belt of the Urals: Composition and mechanism of structure development. *Geotectonics* **27**, 197–207.

Elianov, A. A. & Andreev, G. V. (1991). *Magmatism and metallogeny of platform areas of multistage activation.* Novosibirsk: Nauka.

Elianov, A. A. & Moralev, V. M. (1972). Depth of formation and erosion level of massifs of ultrabasic and alkaline rocks of the Aldan Shield. *Geologiya Rudnykh Mestorozhdeni* **14**, 32–40, (in Russian).

Emelynenko, E. P., Maslovskiy, A. N., Zalishchak, B. L., Kamaeva, L. V. & Fomenko, A. S. (1989). *Regularities of the location of ore mineralizaion at the Kondyor Massif. Geological conditions of the localization of endogenetic ore formation.* Vladivostok: Academy of Sciences, Far Eastern Branch, pp. 100–113 (in Russian).

Ernst, R. E. & Desnoyers, D. W. (2004). Lessons from Venus for understanding mantle plumes on Earth. *Physics of the Earth and Planetary Interiors* **146**, 195–229.

Ernst, R. E. & Desnoyers, D. W. (2009). Corrigendum to 'Lessons from Venus for understanding mantle plumes on Earth' [Phys. Earth Planet Inter. 146 (2004) 195–229]. *Physics of the Earth and Planetary Interiors* (in press).

Ferguson, J. & Currie, L. (1970). Evidence of liquid immiscibility in alkaline ultrabasic dikes at Callender Bay, Ontario. *Journal of Petrology* **12**, 561–585.

Findlay, D. C. (1969). Origin of the Tulameen ultramafic–gabbro complex, southern British Columbia. *Canadian Journal of Earth Sciences* **6**, 399–425.

Garrido, C. J., Bodinier, J.-L. & Alard, O. (2000). Incompatible trace element partitioning and residence in anhydrous spinel peridotites and websterites from the Ronda orogenic peridotite. *Earth and Planetary Science Letters* **181**, 341–358.

Garrido, C. J., Bodinier, J.-L., Dhuime, B., Bosch, D., Chanefo, I., Bruguier, O., Hussain, S. S., Dawood, H. & Burg, J.-P. (2007). Origin of the island arc Moho transition zone via melt–rock reaction and its implications for intracrustal fractionation of island arcs: evidence from the Jijal Complex (Kohistan complex, northern Pakistan). *Geology* **35**, 683–686.

Geoffroy, L. (1998). Diapirisme et extension intraplaque: cause ou conséquence? *Comptes Rendus de l'Académie des Sciences, Sciences de la terre et des planètes* **326**, 267–273.

Gerya, T. V. & Burg, J.-P. (2007). Intrusion of ultramafic magmatic bodies into the continental crust: Numerical simulation. *Physics of the Earth and Planetary Interiors* **160**, 124–142.

Gerya, T. V. & Yuen, D. A. (2003). Characteristics-based marker-in-cell method with conservative finite-differences schemes for modeling geological flows with strongly variable transport properties. *Physics of the Earth and Planetary Interiors* **140**, 295–320.

Godard, M., Bodinier, J.-L. & Vasseur, G. (1995). Effects of mineralogical reactions on trace element redistributions in mantle rocks during percolation processes: a chromatographic approach. *Earth and Planetary Science Letters* **133**, 449–461.

Godard, M., Jousselin, D. & Bodinier, J.-L. (2000). Relationships between geochemistry and structure beneath a palaeo-spreading centre: a study of the mantle section in the Oman ophiolite. *Earth and Planetary Science Letters* **180**, 133–148.

Gurovich, V. G., Zemlianukhin, V. N., Emel'yanenko, E. P., Karetnikov, A. S., Kvasov, A. I., Lazarenkov, V. G., Malitch, K. N., Mochalov, A. G., Prikhodko, V. S. & Stepashko, A. A. (1994). *Geology, petrology and ore content of the Konder massif.* Moscow: Nauka.

Harte, B. (1977). Rock nomenclature with particular relation to deformation and recrystallisation textures in olivine-bearing xenoliths. *Journal of Geology* **85**, 279–288.

Hess, P. C. (1989). *Origin of Igneous Rocks*. Harward University Press, London. 490 pp.

Hippertt, J. F. (1994). Structures indicative of helicoidal flow in a migmatitic diapir (Bação Complex, southeastern Brazil). *Tectonophysics* **234**, 169–196.

Ionov, D. A., Savoyant, L. & Dupuy, C. (1992). Application of the ICP-MS technique to trace-element analysis of peridotites and their minerals. *Geostandards Newsletter* **16**, 311–315.

Irvine, T. N. (1967). The Duke Island ultramafic complex, southeastern Alaska. In: Wyllie, P. J. (ed.) *Ultramafic and Related Rocks*. New York: John Wiley, pp. 84–97.

Irvine, T. N. (1974). Petrology of the Duke Island ultramafic complex, Southeastern Alaska. *Geological Society of America, Memoirs* **138**, 240 .

Jagoutz, O., Müntener, O., Burg, J.-P., Ulmer, P. & Jagoutz, E. (2006). Lower continental crust formation through focused flow in km-scale melt conduits: The zoned ultramafic bodies of the Chilas Complex in the Kohistan island arc (NW Pakistan). *Earth and Planetary Science Letters* **242**, 320–342.

James, O. B. (1971). Origin and emplacement of the ultramafic rocks of the Emigrant Gap area, California. *Journal of Petrology* **12**, 523–560.

Jochum, K. P., Seufert, H. M. & Thirlwall, M. F. (1990). Multi-element analysis of 15 international standard rocks by isotope-dilution spark source mass spectrometry (IDSSMS). *Analytical Chemistry* **331**, 104–110.

Kamenetsky, V. M., Kamenetsky, M. B., Sobolev, A. V., Golovin, A. V., Demouchy, S., Faure, K., Sharygin, V. V. & Kuzmin, D. V. (2008). Olivine in the Udachnaya-East Kimberlite (Yakutia, Russia): types, compositions and origins. *Journal of Petrology* **49**, 823–839.

Kelemen, P. B. (1990). Reaction between ultramafic rock and fractionating basaltic magma: Part I, phase relations, the origin of calc-alkaline magma series, and the formation of discordant dunite. *Journal of Petrology* **31**, 51–98.

Kelemen, P. B. & Ghiorso, M. S. (1986). Assimilation of peridotite in zoned calc-alkaline plutonic complexes: evidence from the Big Jim complex, Washington Cascades. *Contributions to Mineralogy and Petrology* **94**, 12–28.

Khain, V. E. (1985). *Geology of the USSR, first part: Old cratons and Paleozoic fold belts.* Berlin: Borntraeger.

Kharkevich, S. S. & Krot, V. E. (1985). The circular Konder range. *Proroda* **2**, 44–46.

Kononova, V. A., Pervov, V. A., Bogatikov, O. A., Mus-Shumacher, U. & Keller, I. (1995). Mesozoic potassic magmatism of the Central Aldan: Geodynamics and genesis. *Geotectonics* **29**, 224–234.

Lallemant, H. G. A. (1985). Subgrain rotation and dynamic recrystallization of olivine, upper mantle diapirism, and extension of the Basin-and-Range Province. *Tectonophysics* **119**, 89–117.

Lee, W.-J. & Wyllie, P. J. (1997). Liquid immiscibility between nephelinite and carbonatite from 1·0 to 2·5 GPa compared with mantle melt composition. *Contributions to Mineralogy and Petrology* **127**, 1–16.

Mainprice, D. & Silver, P. G. (1993). Interpretation of SKS-wave using samples from the subcontinental lithosphere. *Physics of the Earth and Planetary Interiors* **78**, 257–280.

Malitch, K. N. (1999). *Platinum-group elements in clinopyroxenite–dunite massifs of the East Siberia*. Saint-Petersburg: Saint-Petersburg Cartographic Factory VSEGEI Press..

Malitch, K. N. & Thalhammer, O. A. R. (2002). Pt–Fe nuggets derived from clinopyroxenite–dunite massifs, Russia: a structural, compositional and osmium-isotope study. *Canadian Mineralogist* **40**, 395–418.

Mues-Schumacher, U., Keller, J., Kononova, V. A. & Suddaby, P. J. (1996). Mineral chemistry and geochronology of the potassic alkaline ultramafic Inagli complex, Aldan Shield, eastern Siberia. *Mineralogical Magazine* **60**, 711–730.

Müntener, O., Kelemen, P. B. & Grove, T. L. (2001). The role of H_2O during crystallization of primitive arc magmas under uppermost mantle conditions and genesis of igneous pyroxenites; an experimental study. *Contributions to Mineralogy and Petrology* **141**, 643–658.

Murray, C. G. (1972). Zoned ultramafic complexes of the Alaskan type: feeder pipes of andesitic volcanoes. *Geological Society of America, Memoirs* **132**, 313–335.

Nekrasov, I. Y., Ivanov, V. V., Lennikov, A. M., Oktyabrsky, R. A., Salishak, B. L., Sapin, V. I. & Taskaev, V. I. (1991). Composition of Pt–Fe solid solutions as an indicator of the erosional level of platinum-bearing alkaline–ultrabasic ring intrusives. *Doklady Akademii Nauk SSSR* **321**, 1049–105, (in Russian).

Nekrasov, I. Y., Lennikov, A. M., Oktyabrsky, R. A., Zalishchak, B. L. & Sopin, B. I. (1994). *Petrology and platinum mineralization of the ring alkaline–ultramafic complexes*. Moscow: Nauka.

Nicolas, A. & Poirier, J.-P. (1976). *Crystalline Plasticity and Solid State Flow in Metamorphic Rocks*. London: John Wiley.

Orlova, M. P. (1992). Geology and genesis of the Konder Massif. *Geology of the Pacific Ocean* **8**, 120–132.

Phillips, R. J. & Hansen, V. L. (1998). Geological evolution of Venus: rises, plains, plumes, and plateaus. *Science* **279**, 1492–1497.

Pinkerton, H. & Stevenson, R. J. (1992). Methods of determining the rheological properties of magmas at subliquidus temperatures. *Journal of Volcanology and Geothermal Research* **53**, 47–66.

Pushkarev, Y. D., Kostoyanov, A. I., Orlova, M. P. & Bogomolov, E. S. (2002). Peculiarities of the Rb–Sr, Sm–Nd, Re–Os and K–Ar isotope systems in the Kondyor massif: mantle substratum, enriched by PGE. *Regional Geology and Metallogeny* **16**, 80–91, (in Russian).

Ranalli, G. (1995). *Rheology of the Earth*. Chapman & Hall, London. 413 pp.

Ruckmick, J. C. & Noble, J. A. (1959). Origin of the ultramafic complex at Union Bay, southeastern Alaska. *Geological Society of America Bulletin* **70**, 981–1017.

Schermerhorn, L. J. G., Priem, H. N. A., Boelrijk, N. A. I. M., Hebeda, E. H., Verdurmen, R. H. & Verschure, E. A. T. (1978). Age and origin of the Messejana Dolerite fault–dike system (Portugal and Spain) in the light of the opening of the North Atlantic Ocean. *Journal of Geology* **86**, 299–309.

Schmidt, M. W. & Poli, S. (1998). Experimentally based water budgets for dehydrating slabs and consequences for arc magma generation. *Earth and Planetary Science Letters* **163**, 361–379.

Shcheka, G., Lehmann, B., Gierth, E., Gömann, K. & Wallianos, A. (2004). Macrocrystals of Pt–Fe alloy from the Kondyor PGE placer deposit, Khabarovskiy Kray, Russia: trace-element content, mineral inclusions and reaction assemblages. *Canadian Mineralogist* **42**, 601–617.

Silva, P. F., Marques, F. O., Henry, B., Mateus, A., Lourenco, N. & Miranda, J. M. (2004). Preliminary results of a study of magnetic properties in the Foum-Zguid dyke (Morocco). *Physics and Chemistry of the Earth* **29**, 909–920.

Stolper, E. (1980). A phase-diagram for mid-ocean ridge basalts— Preliminary results and implications for petrogenesis. *Contributions to Mineralogy and Petrology* **74**, 13–27.

Suhr, G. (1999). Melt migration under oceanic ridges: inference from reactive transport modeling of upper mantle hosted dunites. *Journal of Petrology* **40**, 575–600.

Sun, S. S. & McDonough, W. F. (1989). Chemical and isotopic systematics of oceanic basalts: implications for mantle composition and processes. In: Saunders, A. D. & Norry, M. J. (eds) *Magmatism in the Ocean Basins. Geological Society, London, Special Publications* **42**, 313–345.

Sushkin, L. B. (1995). Characteristic features of the native elements of the Kondyor deposit. *Tikhookeanskaya geologiya* **14**, 97–102, (in Russian).

Taylor, H. P. J. (1967). The zoned ultramafic complexes of southeastern Alaska. In: Wyllie, P. J. (ed.) *Ultramafic and Related Rocks*. New York: John Wiley, pp. 97–121.

Turcotte, D. L. & Schubert, G. (2002). *Geodynamics*. Cambridge University Press, Cambridge. 456 pp.

Veksler, I. V., Nielsen, T. F. D. & Sokolov, S. V. (1998). Mineralogy of crystallized melt inclusions from Gardiner and Kovdor Ultramafic Alkaline Complexes: Implications for carbonatite genesis. *Journal of Petrology* **39**, 2015–2031.

Waters, F. G. (1987). A suggested origin of MARID xenoliths in kimberlites by high pressure crystallization of an ultrapotassic rock such as lamproite. *Contributions to Mineralogy and Petrology* **95**, 523–533.

Wilson, L. & Head, J. W., III (2007). An integrated model of kimberlite ascent and eruption. *Nature* **447**, 53–57, doi:10.1038/nature05692.

Wyllie, P. J. (1967). *Ultramafic and Related Rocks*. New York: John Wiley.

Zemlyanukhin, V. N. & Prikhodko, V. S. (1997). Structures and petro-textures of the ultrabasic cores of ring massifs in the Russian Far East. *Geology of the Pacific Ocean* **13**, 689–700.

APPENDIX: GPS LOCATION OF SAMPLES MENTIONED IN TEXT AND TABLES

Sample	Latitude N			Longitude E		
no.	deg	min	sec	deg	min	sec
K1	57	35	59·6	134	41	16·2
K2	57	35	27·6	134	41	25·9
K16	57	33	18·6	134	40	07·1
K18	57	33	28·6	134	39	43·2
K19	57	34	53·1	134	36	42·3
K28	57	34	44·7	134	38	22·9
K29	57	34	47·1	134	37	56·1
K37	57	36	41·2	134	40	26·1
8192	57	35	05·1	134	38	14·8
8198	57	35	17·1	134	37	54·5
8201	57	35	31·2	134	37	27·7
8216	57	35	45·0	134	37	05·0
8226	57	35	41·1	134	37	10·6
8235	57	35	57·0	134	36	37·3
8353	57	34	55·3	134	37	15·3
8258	57	35	00·3	134	37	58·4
8266	57	36	20·8	134	38	45·2
8276	57	36	22·3	134	37	51·1
8302	57	34	57·9	134	42	36·1
8304	57	34	39·3	134	38	49·1
8305	57	34	35·4	134	38	45·9
8308	57	34	30·2	134	38	45·2
8319	57	34	19·8	134	38	45·3
8323	57	34	14·7	134	38	46·2
8375	57	34	24·8	134	37	47·2
8385	57	34	05·9	134	36	41·4
8388	57	34	06·0	134	38	42·3
8398	57	33	57·8	134	38	39·2
8403	57	33	48·7	134	38	39·3
8408	57	33	40·9	134	38	34·6
8409	57	33	39·2	134	38	41·1
8439	57	34	23·3	134	42	22·0
8443	57	36	11·3	134	40	17·2
8486	57	34	50·8	134	39	42·9
8491	57	34	51·0	134	39	43·0

Core samples (Table 1) are from non-located drills within the koswite and phlogopite-rich stockwork (Fig. 2), courtesy of the Artel Amur mining company